

POLITECNICO DI TORINO

Master's Degree in Biomedical Engineering

Master's Thesis

**Development of interactive
algorithms to infer cellular retinal
functional properties on a
closed-loop CMOS-MEA platform**



Supervisor:
prof. Danilo Demarchi

Co-supervisor:
Dr. Luca Berdondini

Candidate:
Sara Zaher

A.A. 2017/2018

Contents

Abstract	VII
Sommario	IX
1 Introduction	1
2 Visual information processing in the eye	5
2.1 The retina	6
2.1.1 A highly organized layered cellular structure	7
2.1.2 Structure-function relationship of retinal cellular organization	7
2.2 Neurons and synapses	9
2.3 Functional properties of retinal ganglion cells	12
2.3.1 Classification and preferential responses of RGCs	12
2.3.2 Spatial integration of visual stimuli: Receptive Fields	13
3 Electrophysiology: the study of neuronal bioelectrical activity	21
3.1 Monitoring the bioelectrical activity of neuronal tissue	22
3.1.1 Single neuron measurements	23
3.1.2 From single neurons to networks	25
3.1.3 Identification of single units in extracellular recordings	28
3.2 Investigating the input/output properties of neural networks	32
3.3 Closing the loop: real-time interaction with neuronal networks	32
3.3.1 Closed-loop architectures in brain machine interfaces	33
4 Data processing	35
4.1 Detection of sub-millisecond correlated spiking activities	36
4.2 Clustering of redundant spiking activity	39
4.3 Generation of simulated spiking activity	41
4.4 Preferential response of the identified units	42
4.5 Estimation of RGCs RF	44

5 Results	47
5.1 Data reduction	47
5.1.1 Validation on simulated spike trains	48
5.1.2 Performance on experimental datasets	50
5.2 RGCs classification	52
5.3 Estimation of RF RGCs	54
6 Conclusion	61
6.1 Discussion	63
Annex I Experimental setup	65
Bibliography	70

Acknowledgements

I would like to thank all the people who contributed in some way to the work described in this thesis.

First and foremost I want to thank my supervisor prof. Danilo Demarchi for his support and for giving me the possibility to expand my knowledge in the fascinating field of neuroscience and to develop this master thesis project.

I would sincerely thank also my co-supervisor Dr. Luca Berdondini who accepted and welcomed me into his NetS³ lab and encouraged me during the months spent in the lab.

I am deeply grateful also to Davide Lonardoni for his patience, motivation, wide knowledge and most of all for his guidance, which helped me in all the time of research and writing of this thesis. I have been extremely lucky to have a person who cared so much about my work, and who responded to my questions and doubts so promptly. I am particularly grateful also to Fabio Boi for his availability and for the assistance that gave me during all the development of this work.

I would also like to thank all the other members of the NetS³ lab Gian Nicola Angotzi, Aziliz Lecomte, Lidia Giantomasi and Stefano Zordan for providing a friendly and cooperative atmosphere in the lab and for making my time spent at the lab very pleasant.

Finally, I must express my very profound gratitude to my parents for providing me with unfailing support and continuous encouragement throughout my years of study and through the process of researching and writing this thesis. This accomplishment would not have been possible without them. Thank you.

Abstract

The retina is a major sensory processing circuit for humans and as the overall nervous system, it is a complex and hierarchical large network of cells consisting of different types of neurons. These cells communicate with each other through biochemical and bio-electrical signals that, at the circuit level, lead to the encoding of different features of the visual inputs. To understand this process many studies based on electrophysiological recordings have been conducted on single-cells or on a restricted pool of cells. Only with the recent technological developments, such as the new generations of high-density microelectrodes arrays (HD-MEA) that exploit CMOS (Complementary Metal-Oxide-Semiconductor) technology, we have reached the capability of monitoring the light-evoked responses of several thousands of retinal ganglion cells (RGCs) in individual retinas. In this master thesis I aimed at advancing these experimental capabilities by contributing in the development of a closed-loop platform for investigating cellular retinal functional properties. Originally, it will allow to study these cellular properties by stimulating the retina according to its internal state associated with the spontaneous electrical activity. Indeed, even though HD-MEAs provide an accurate description of the neuronal activity, the implementation of closed-loop platforms that can exploit their spatial-spatiotemporal resolution remains very challenging due to the demanding computations required for handling the large recorded data stream at millisecond range latencies. A recently proposed hardware architecture that exploits the FPGA/CPU resources of a Xilinx ZedBoard Zynq-7000 was introduced to perform data pre-processing tasks, such as signal conditioning, filtering and spike detection, with a maximum latency of 2 ms. In this thesis, I have extended the capabilities of this closed-loop platform, first by implementing a pseudo-real-time algorithm that removes redundant information in the recorded spiking activity induced by the tight spacing among adjacent electrodes of HD-MEA. This algorithm consists in a clustering procedure that identifies spatial and temporal correlated spiking units. In my work, this approach has been also extensively tested and validated in HD-MEA recordings of *ex vivo* mouse retina. Next, I have implemented a second closed-loop algorithm that controls visual stimuli to infer the major functional properties of retinal ganglion cells. In detail, based on the spiking response to white and black stimuli, the algorithm classifies the units in ON- or OFF-type retinal ganglion cells. Finally, in the last part of my study, I evaluated a potential approach for estimating the retinal ganglion cells receptive field size in real-time. State-of-the-art approaches allowing for an accurate and precise estimation of the receptive fields are very time-consuming. On the contrary, the approach that I have developed aims at minimizing the experimental time and the amount of data required for estimating the receptive fields of retinal ganglion cells. All in all, the interactive algorithms that I have designed, implemented and validated in this work against experimental data provide a new suite of tools to characterize the retinal circuit and to investigate how it implements visual information processing. In perspective, these algorithms can be extended to other experimental preparations and high-density recording devices, such as high-density implantable probes for *in vivo* studies. Part of the outcomes of this master thesis work were submitted to the IEEE-NER 2019 conferences.

Sommario

La retina è un importante circuito di elaborazione sensoriale per gli esseri umani ed essendo parte del sistema nervoso, è formata da una complessa e gerarchica rete di cellule composta da diversi tipi di neuroni. Queste cellule comunicano tra loro attraverso segnali biochimici e bioelettrici che portano alla codifica di diverse caratteristiche degli input visivi. Per comprendere questo processo sono stati condotti molti studi basati su registrazioni elettrofisiologiche di singole cellule o di un insieme ristretto di cellule. Solo grazie ai recenti sviluppi tecnologici, come le nuove generazioni di matrici di microelettrodi ad alta densità (HD-MEA) che sfruttano la tecnologia CMOS (Complementary Metal-Oxide-Semiconductor), oggi è possibile monitorare le risposte di migliaia di cellule gangliari retiniche (RGC) evocate da stimoli visivi. L'obiettivo di questo lavoro è arricchire queste capacità sperimentali contribuendo allo sviluppo di una piattaforma a circuito chiuso per lo studio delle proprietà funzionali delle cellule retiniche attraverso stimolazioni dipendenti dall'attività istantanea di tale circuito. Tuttavia, anche se gli HD-MEA forniscono una descrizione accurata dell'attività neuronale, l'implementazione di piattaforme a circuito chiuso in grado di sfruttare la loro alta risoluzione spazio-temporale rimane molto impegnativa a causa dell'elevato costo computazionale richiesto per gestire il flusso di dati in latenze al millisecondo. Recentemente è stata proposta un'architettura hardware che sfrutta le risorse FPGA/CPU di una Xilinx ZedBoard Zynq-7000, in grado di pre-processare i dati, come il condizionamento del segnale, il filtraggio e rilevamento di spike, con una latenza massima di 2 ms. In questa tesi, ho esteso le capacità di questa piattaforma a circuito chiuso, implementando un algoritmo che attraverso un procedimento di clustering identifica le unità attive correlate e rimuove le informazioni ridondanti nell'attività di spike registrata indotta dall'elevata vicinanza tra gli elettrodi adiacenti degli HD-MEA. Sebbene sia adatto ad altre preparazioni sperimentali, questo approccio è stato ampiamente testato e validato nelle registrazioni HD-MEA della retina *ex vivo* di topo. Successivamente, ho implementato un secondo algoritmo a circuito chiuso che controlla gli stimoli visivi per inferire le principali proprietà funzionali delle cellule gangliari retiniche. In particolare, in base alla risposta agli stimoli bianchi e neri, l'algoritmo classifica le unità in cellule gangliari retiniche di tipo ON o OFF. Infine, nell'ultima parte del mio studio, ho valutato un potenziale approccio per stimare le dimensioni del campo recettivo delle cellule gangliari retiniche in tempo reale. Gli approcci allo stato dell'arte richiedono molto tempo per una stima accurata e precisa dei campi ricettivi. Pertanto, l'approccio che ho sviluppato mira a ridurre al minimo il tempo sperimentale e la quantità di dati richiesti per la caratterizzazione dei campi recettivi. Gli algoritmi interattivi che ho progettato, implementato e validato su dati sperimentali forniscono una nuova serie di strumenti per la caratterizzazione e l'analisi, in tempo reale, dell'elaborazione delle informazioni visive eseguite dal circuito retinico. Infine questi algoritmi possono essere estesi ad altri preparati sperimentali e ad altri dispositivi di registrazione ad alta densità, come ad esempio le sonde impiantabili ad alta densità per studi *in vivo*. Parte dei risultati ottenuti in questa tesi di laurea sono stati inviati come contributo originale alla conferenza IEEE-NER 2019.

1 Introduction

The basic challenge in neuroscience is to understand how tens of billions of neurons, which are the fundamental elements of the brain, interact with each other giving rise to all the functions of the brain that allow us to receive sensory inputs, act, learn and remember. The mechanism underlying the functioning of the nervous system can be grossly described in the following way: after receiving a sensory stimulus, a primary sensory neuron generates a signal, which is transmitted to other neurons along the nervous system until it reaches its target effector organs or glands. Thus, a fundamental problem in neuroscience is to understand how neuronal activity encodes the sensory signals that are continuously received from the external world.

To study how brain circuits process sensory information at the network level, the retina represent a system of great interest in neuroscience because of its accessibility and the possibility of investigating its input/output functions in a natural environment, i.e., by providing natural visual stimuli [1]. The retina is a major sensory processing circuit for humans and as such, visual disabilities due to retinal pathologies can radically degrade the quality of life of people. In this respect, advancing in understanding its visual information processing has strong implications for R&D on strategies for vision restoration, including retinal prosthetics and cell-/drug-based therapies. During development, the retina grows as an anatomical protrusion of the central nervous system (CNS). As such, it consists of a complex network of diverse neuronal cells that are arranged in a few well-organized layers: photoreceptors, bipolar cells, horizontal cells, amacrine cells and retinal ganglion cells. These cells communicate with each other through biochemical and bioelectrical signals that, at the circuit level, lead to the encoding of different features of the visual inputs. Differently from other brain areas, nearly all neurons in the retina communicate through graded potentials except for the retinal ganglion cells and a few subtypes of amacrine cells that are able to generate action potentials [2].

While for decades the retina has been studied with electrophysiological recordings from single-cells or from a restricted pool of cells, recent technological advancement culminated in the unique possibility of simultaneously monitoring the

light-evoked responses of several thousands of retinal ganglion cells (RGCs) in individual retinas [3], [4]. This result was achieved with new generations of high-density microelectrodes arrays (HD-MEA) that exploit CMOS (Complementary Metal-Oxide-Semiconductor) technology to integrate several thousands of closely spaced microelectrodes [5] in active devices with on-chip read-out circuits.

For decades neuroscientists studied the nervous system in an open-loop manner, i.e., by analysing the output of neurons in response to a given external stimulus independently from the state of the neuronal network. This strategy has provided valuable insights in understanding the transient response of isolated neuronal circuits at cellular level. However, it may not apply in physiological operating conditions. Indeed, each neuron in the nervous system integrates the external information with the spiking activity of thousands of other neurons that represent the state of the network. For instance, it has been proven that the retinal processing is based on non-linear feedback controls [6],[7]. In this perspective neuroscientists started to design closed-loop systems that could control and eventually exploits the instantaneous neural activity after specific stimulation to investigate in real-time the neuronal processing of sensory information.

Closed-loop manipulations have the unique power of revealing the high non-linearity of neuronal responses and can be used to investigate several interesting phenomena: the neuronal homeostatic adaptation, by controlling the stimulation current that maintain the average firing rate at a desired inter-spike-interval [8], the neuronal and network plasticity, by correlating the spike timing between sets of arbitrary neurons [9], the excitability of neurons, by controlling their instantaneous response probability [10], the network dynamic, by controlling the timing of network bursts in cortical cultures [11], and visual processing by identifying different visual stimulus patterns that yield the same neuronal response [12].

In the retina, closed-loop approaches can contribute to disentangle the operating principles underlying visual processing. Indeed, the retina represents a reduced and well-organized neuronal system in which retinal ganglion cells, i.e., the output neurons of the retina, combine and compare both in space and time features of the stimulus from contiguous region of the visual field called receptive fields (RFs). The RF is defined as the portion of the visual field in which a light stimulus produces a modulation of the spiking activity upon the application of a visual stimulus. The RF properties may change depending on a certain number of factors that include, but are not limited to, ambient luminance and adaptation to stimuli. Therefore a description of their characteristics is of primary and essential importance for understanding how the visual information is encoded by the retina.

The main contribution of this work, indeed, consists in the development of hardware embedded algorithms in a closed-loop platform for investigating cellular retinal functional properties. These algorithms exploit the instantaneous firing of

the retinal ganglion cells to reduce the time required for experimental investigation. The hardware platform used in this work exploits the FPGA/CPU resources of a Xilinx ZedBoard Zynq-7000 that have been proven to handle the data stream of HD-MEAs [13]. In particular, this platform can perform pre-processing tasks, such as signal conditioning, filtering and spike detection, with a maximum latency of 2 ms allowing to record and stimulate retinal networks according to their spontaneous electrical activity. By exploiting these capabilities, I worked on implementing novel approaches to infer cellular properties based on their dynamical response to closed-loop controlled visual stimuli.

HD-MEAs record RGCs spiking activity from 4096 electrodes simultaneously and thus provide an accurate description of the neuronal activity. However, this has a price of a very demanding computational cost required to analyze the data stream of thousands of electrodes. Consequently, the implementation of closed-loop algorithms that can exploit the spatiotemporal resolution of HD-MEAs with a maximum latency of a few tenths of milliseconds is still a computational challenge.

A simple strategy to reduce this computational cost concerns the number of electrodes that has to be simultaneously analysed. Indeed, it has been noticed that, in retinal preparations, the spike trains recorded by adjacent electrodes in HD-MEA systems, may include redundant information as a consequence of the tight spacing between electrodes. Thus, I exploited the closed-loop platform for the identification of duplicated spikes in spatially adjacent electrodes. To avoid subsequent redundant analysis, a leader electrode (the one with the highest number of spikes recorded) is selected among those electrode that are consistently recording coincident spiking activities and all the remaining electrodes were discarded. To validate this approach, I generated simulated correlated spike trains according to a pre-determined probability of firing acting as ground-truth and then I tested the performance of the algorithms on real dataset. For the experimental phase the close-loop configuration is exploited in order to save time and memory estimating the amount of data to record for achieving a stable configuration of clustered channels.

Next, I have implemented a second closed-loop algorithm that controls visual stimuli to infer major functional types of RGCs. In detail, based on the spiking response to white and black stimuli, the algorithm classifies the representative electrodes identified with the first algorithm in ON- or OFF-type RGCs responses. These two cell-types of RGCs transiently activated by an increase (ON-type) or decrease (OFF-type) in light intensity, respectively. To do so, the algorithm controls a digital light projector (DLP) to visually stimulate the retina. After projecting each light stimulus, the algorithm counts the number of spikes for each leader electrode and computes the difference of their firing rate during the black and the white phase, with respect to the spontaneous activity. Then, each leader electrode

is classified as ON if it increases the firing rate during a white flash stimulus, and OFF vice-versa.

Finally, considering that state-of-the-art approaches are highly time-consuming for an accurate and precise estimation of the RFs [14], [15], [16] the approach that I tested in this work aims at minimizing the experimental time and the amount of data required for the receptive fields characterization. This is implemented by using a white-black curtain image stimuli whose white edge spans the RF from left to right and vice versa the visual field.

Structure of the thesis

In the first Chapter, I report a general overview of the visual system with a particular focus on the retina and its functional properties. The principal functional characteristics of retinal ganglion cells, as their preferential response to visual stimulation and the concept of receptive field, are described in details.

The second Chapter reports an overview on the electrophysiology approaches developed in neuroscience to acquire the bioelectrical activity of neuronal circuits, and in particular of the retinal circuit, with the goal of investigating their operating principles. In the same Chapter, I included the description of the closed-loop hardware architecture used as a starting point of my work.

The third Chapter describes my original contribution and provides a complete description of the implemented interactive algorithms.

The results obtained are presented in Chapter 4 and discussed in Chapter 5. Finally, Annex I reports a technical description of the experimental techniques and setups used in this thesis.

2 Visual information processing in the eye

The eye is the sensory organ dedicated to acquire and render visual cues about the external world to an organism. To fulfil this task, the eye acts as a tunable optical instrument that focuses visual images onto a photosensitive tissue called retina, located in the inner-most part of the eye. Importantly, the retina is the neuronal circuit that evolution has refined to transduce variations in light intensity into the language of the brain, i.e. electrical neural impulses [17].

As shown in Figure 2.1, the general structure of a vertebrate eye, despite species-specific features, consists of the following components (from the outermost to the innermost):

- *Cornea*: a transparent spherical membrane that covers the front part of the eye to let the light enter.
- *Iris*: a two-layer pigmented muscle tissue located behind the cornea that, as an optical diaphragm, regulates the amount of light reaching the retina by modifying the size of the pupil. The iris is also responsible for eye coloring.
- *Pupil*: an opening located in the iris centre that, similarly to the aperture of an optical diaphragm, allow light passage. The size of the pupil, and thus the amount of light entering in the central part of the eye, is finely controlled by the iris.
- *Eye lens*: a convex lens made of transparent jelly that focus the ray lights of an image onto the retina. Ciliary muscles hold in position the eye lens and tune its curvature to maintain the focal point onto the retina plane.
- *Sclera*: a fibrous membrane that constitutes the white external posterior part of the eye and ensures the mechanical resistance of the eye.
- *Choroid*: a connective tissue layer surrounding the internal eye that provides oxygen and nutrients through rich arborizations of blood vessels.

- *Retina*: the light-sensitive tissue of the eye. It maintains its position in the eye thanks to the pressure of the vitreous body, a jelly fluid that fills the eye-bulb and pushes the retina onto the internal wall of the eye protecting it from mechanical shocks and traumas. In primates [18], in some subspecies of fish [19] and birds [20], the retina exhibits an additional highly specialized structure, called fovea, devoted to sharp central vision, i.e. the accurate discrimination of details located in the central part of the visual field. However, other mammals such rats and mice lack this area and thus their central vision resembles the peripheral vision of fovea-equipped animals.
- *Optic nerve*: a nerve composed of approximately one million axons that transmit the bioelectrical activity of retinal ganglion cells, the output neurons of the retina, to the brain.

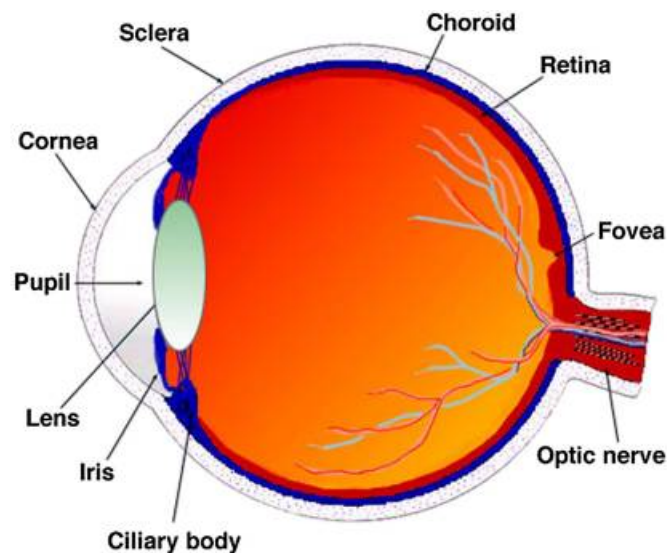


Figure 2.1: Principal structural components of the vertebrate eye involved in the sensory processing of visual input. Picture adapted from [17].

Consistent with its status as a part of the central nervous system, the retina comprises a complex cellular circuitry that is described in details in the following part.

2.1 The retina

The retina is the neuronal tissue in charge of phototransducing and pre-processing visual stimuli: it senses variations of light, extract relevant features about the

visual scene (e.g. motion detection) and encodes this information into bioelectric signals that are then sent to the brain through the optic nerve. Despite its location, the retina is considered part of the central nervous system (CNS) because it consists of nerve cells originating in the developing brain.

2.1.1 A highly organized layered cellular structure

The retina consists of two principal cellular layers, namely the pigmented epithelium, a thin layer in contact with the choroid, and the *sensory retina*, containing all the nerve cells devoted sensory and processing, that connect the retina with the vitreous body, see Figure 2.2.

In detail, the pigmented epithelium is organized in a single layer of densely packed non-neuronal cells containing large amounts of black pigment, the melanin, which absorb all the photons reaching the back of the eye. Despite its simple structure, the pigmented epithelium has other essential functions as:

- active transport of the metabolites;
- constitution of the blood-retinal barrier;
- regeneration of photopigments of the photoreceptors;
- phagocytosis of the outer layer of photoreceptor cells.

The *sensory retina*, instead, is a multi-layered structure in which each layer is populated by a specific population of nerve cells, suggesting a function-structure relationship in retinal information processing. In detail, the retina contains six major types of nervous cells (from the outermost part to the innermost): rods and cones, horizontal cells, bipolar cells, amacrine cells and retinal ganglion cells whose elongated axons give rise to the optic nerve. These cells do not merely transfer the whole visual scene to the brain in a pixel-by-pixel fashion, but they rather combine and integrate signals from small patches of the visual field to generate a low-dimensional representation.

2.1.2 Structure-function relationship of retinal cellular organization

To each population of cells has been attributed a peculiar functional role in the retinal visual processing:

Rods and cones are the photoreceptors, i.e., the light-sensitive cells of the retina that convert light energy into electrochemical signals. In human retina, the cones outnumber the rods in the central area of the retina called macula

and allow the perception and recognition of colors during daylight vision (photopic vision).

There are three types of cones, each of which contains a pigment sensitive to particular wavelengths in the visible spectrum. Notably, there are only three types of pigment with absorption peaks at 420, 530 and 560 nm, that correspond respectively to blue, green and red light colors. Conversely, a reciprocal rod-to-cone ratio characterizes the medium and peripheral area of the retina. Rods have higher sensitivity to light compared to cones, and they can sense as little as single photons. As such, rods are essential in night vision (scotopic vision). These cells continuously release glutamate, a neurotransmitter, except when activated by light.

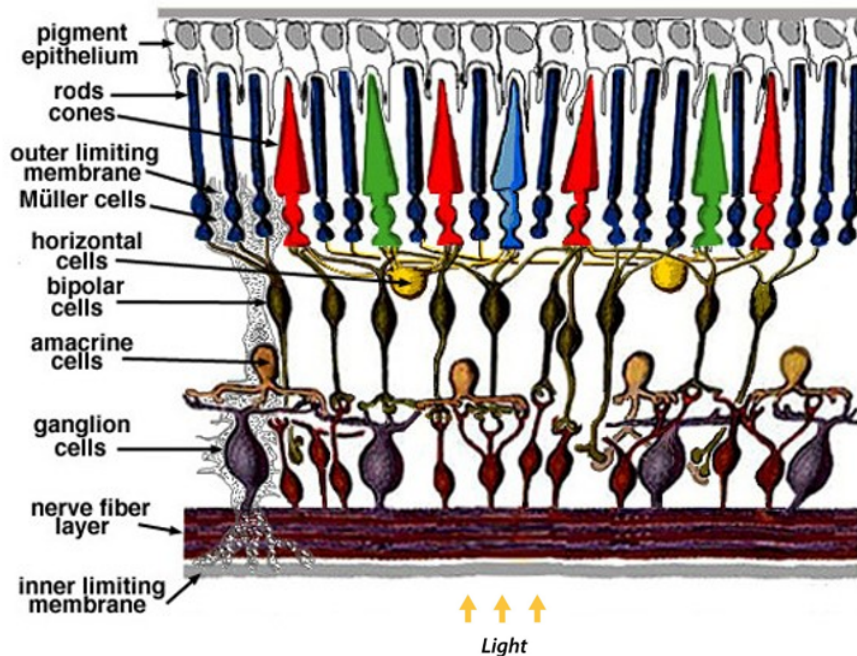


Figure 2.2: Schematic representation of a vertical section of the retina showing its organization in cellular layers. Note that the light travels through all the cellular layers before reaching the photoreceptors. Picture adapted from [17]

Bipolar cells are neurons that synapse either with cones or rods and they can also receive inputs from horizontal cells. They transmit the information collected to the retinal ganglion cells directly or indirectly through the amacrine cells.

Horizontal cells are neurons which connect the photoreceptors laterally and integrate information received from multiple cones or rods and provide inhibitory feedback to the photoreceptors. The principal function of these cells is to provide adaptation to high or low light ambient luminance.

Amacrine cells are inhibitory neurons typically with very short axons. Similarly to horizontal cells, they horizontally integrate the inputs received from bipolar cells, or other amacrine cells, and transmit their output to the retinal ganglion cells.

Retinal Ganglion Cells (RGCs) are the principal population of cells in the visual system capable of generating action potentials: they spontaneously fire spikes at a basal firing rate when they are in a rest condition [21]. When RGCs are excited, they increase their firing rate; instead, an inhibition results in silencing the spiking activity. They receive visual information from the photoreceptors through bipolar and amacrine cells. RGCs can be mainly distinguished in M-type cells (Magnae) and P-type cells (Parvae): the first are connected to a large number of cones and rods and, for this reason, they are able to provide information on the movement of an object or on rapid variations in the light context. P-type cells are instead connected with fewer receptors and provide information on the shape and color of an object. The axons of retinal ganglion cells give rise to the optic nerve and constitute the unique pathway of visual information transmission between the retina and the brain.

The retina has an active role in encoding and pre-processing visual information. In fact, the retina extracts and transmits to the brain only relevant features of the visual field, mostly associated with local variations of light. Indeed, the visual scene is not presented to the retina statically, but through constant and continuous micro-movements, called saccades, that are suggested to improve visual acuity as a consequence of the variation in light intensity induced by the spatial movement [22].

2.2 Neurons and synapses

In vertebrates the retina and the optic nerve originate as external outgrowth of the brain during the embryonic development. The retina is therefore considered as a part of the Central Nervous System (CNS) and, as such, contains neurons, i.e., the fundamental units that constitute the CNS and the Peripheral Nervous System

(PNS). As shown in Figure 2.3, each neuron is a cell that consists of a main body, the soma, and two different types of arborizations, the dendrites and the axons.

Soma contains the nucleus and the cellular organelles. It receives electrical signals from the dendrites, integrates them and eventually generate a transient variation in the membrane potential that is transmitted through the axon.

Dendrites have the task of receiving information from other neurons and transmitting it to the cell body in the form of electrical signals. The branched arborization, which characterizes the dendrites, increases the surface area for receiving information.

Axon is the extension of the soma of a neuron. It is usually one and generally is wrapped in a myelin sheath, a lipid substance that protect and electrically insulate nerve fibres. In between adjacent myelin sheaths, dedicated regions called nodes of Ranvier, boost the electrical signal to cope with electrical attenuation along the axon. The insulation increase the speed and the reliability of transmission of the nerve impulse. Myelinated axons are typically found in peripheral nerves (motor and sensory neurons), whereas non-myelinated neurons are found in the brain and spinal cord.

Neurons are surrounded by a cell membrane that keep the extracellular environment and the cytoplasm separated. Through membrane channels that control the exchange of the charged molecules, the neuron is able to maintain a voltage difference between the external solution and the intracellular one of around 60-90 mV. The most important characteristic of a neuron is the ability to modulate this electrical potential to generate electrical impulses named action potentials (or spikes). Specifically, in mammals action potentials are a fast (about 1 ms) and large (about 100 mV) depolarization and repolarization of the cell membrane. The action potential that propagates along the axon is transmitted to another neuron or to effector organs (muscles and glands) through specialized junctions, called synapses. The neurons that transfer the nerve impulse towards the synapse are the presynaptic neurons, instead those that transfer it downstream of the synapses are the postsynaptic neurons.

The axon terminal (or synaptic bouton) of the presynaptic neuron is a complex structure containing a chemical mediator (neurotransmitter) that accumulates in small vesicles. Once the action potential arrives at the pre-synaptic site activate the release of neurotransmitter from the synaptic bouton into the synaptic cleft. Neurotransmitters bind to postsynaptic synaptic receptors that by transiently opening ion channels modulate the membrane potential of the post-synaptic neuron. Depending on the effect, some synapses are called excitatory because their activation increase the membrane potential of the post-synaptic neurons.

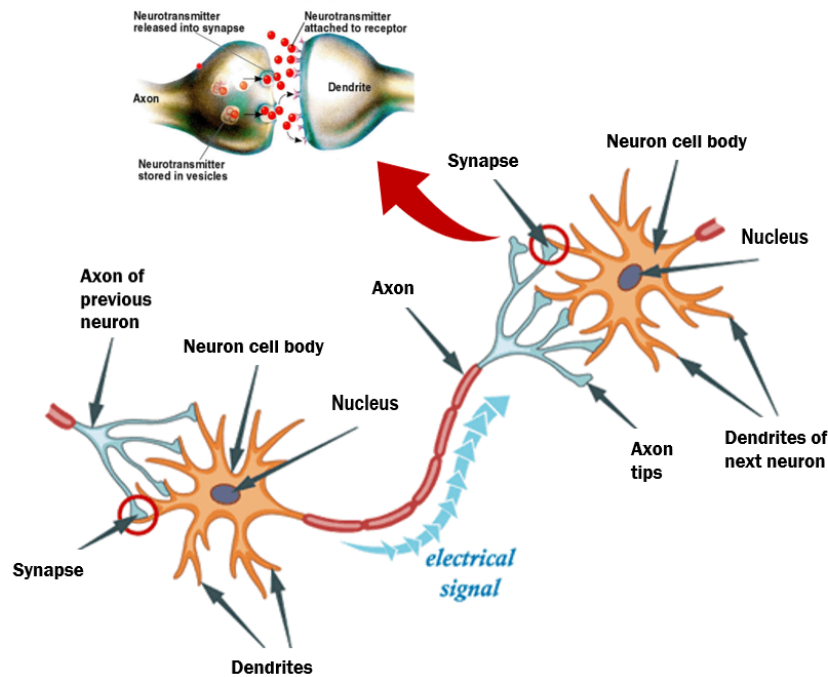


Figure 2.3: Representation of a neuron and the synaptic connection. Image adapted from [23].

Conversely, synapses that determine a decrease of the post-synaptic membrane potential are called inhibitory synapses.

To study how brain circuits process information at the network level, the retina represents a system of great interest in neuroscience because of its accessibility and the possibility of investigating its input/output functions in a natural environment, i.e., by providing natural visual stimuli.

Differently from other brain areas, while all the nervous cells in the retina communicate through graded potential, only the retinal ganglion cells are able to generate action potential.

Typically, the retina can be studied with extracellular recordings by flattening the curved neuronal tissue after dissection. In this way, the RGC layer can be put in contact with an array of recording electrodes to record the spiking activity of RGCs and, thus, the information about the visual field transmitted through their spike trains to downstream brain areas.

2.3 Functional properties of retinal ganglion cells

The Retinal Ganglion Cells (RGCs) send a diverse set of parallel, highly processed images of the world to higher visual areas in the brain [24]. Thus, the retina is not merely a light detecting circuit, but rather a feature detector and specialized encoder for downstream brain areas. RGCs collect information about the visual scene from bipolar cells and amacrine cells as chemical messages sensed by receptors on the ganglion cell membrane. Transmembrane receptors, in turn, transform the chemical messages into intracellular electrical signals which are integrated within ganglion-cell dendrites and cell body, producing spike trains. Through these spike trains the RGCs are able to communicate information about the visual scene to downstream areas of the brain. Based on their function, i.e., their response to visual stimuli, different cell-types of RGCs can be distinguished [4].

2.3.1 Classification and preferential responses of RGCs

According to the different features of the visual scene as color, size, direction and speed of motion, studies in vertebrate retina [24] discovered different types of RGCs depending on their preferential response to visual images features. Even so, signals detected by RGCs may not have a unique interpretation. Equivalent signals might result from an object changing brightness, changing shape, or moving. It is up to the brain to determine the most likely interpretation of detected events and, in the context of events detected by other RGCs, take appropriate action [25].

Even though each RGC encode slightly different features of the visual scene, they can be classified in a few groups according to their preferential response to visual stimulation. The simplest stimuli consist of black and white full-field flashes and allow to classify nearly all retinal ganglion cells into three principal functional sub-types, namely ON, OFF, ON-OFF retinal ganglion cells. In particular, the ON-RGCs (OFF-RGCs) are excited by increments (decrements) of light intensity; instead, the ON-OFF RGCs respond to both positive and negative changes [26] (see Figure 2.4).

In addition, each vertebrate RGC is tuned for objects of a different size, reflecting in part the variable dendritic span of retinal ganglion cells. A measure for the size selectivity in RGCs is the contrast sensitivity as the activation of retinal ganglion cells is a function of both the difference in brightness between the light and dark phases of the bar pattern (contrast) and the bar width (spatial) [25].

Further, some retinal ganglion cells provide information about the direction of a moving object or scene. Directional selective (DS) RGCs respond to stimuli moving in a preferred direction and are inhibited by stimuli moving in the opposite direction. The preferred direction is independent of the nature of the object, which can be either bright or dark, a simple object such as a small spot, or a complex

object, such as a drifting grating. The first evidence for such retinal computation was established in the rabbit retina [27].

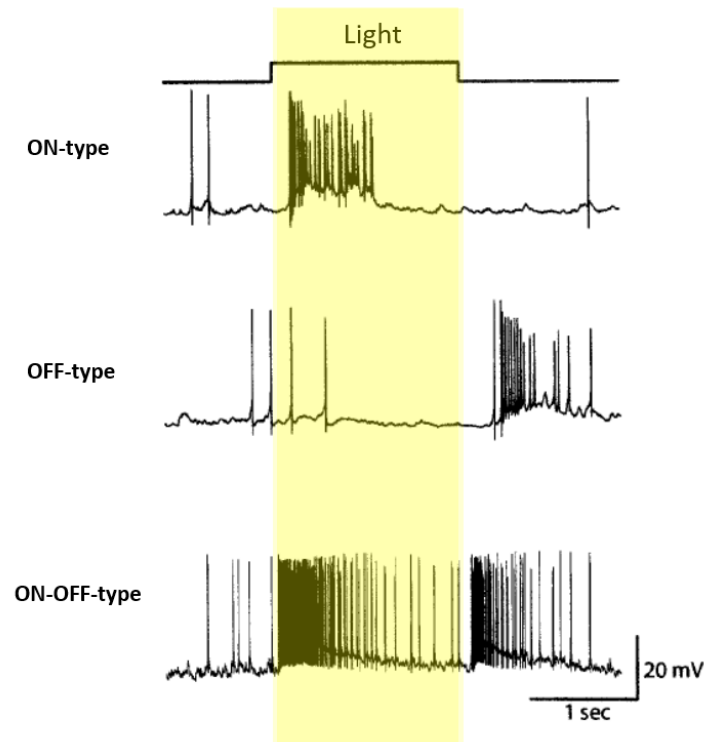


Figure 2.4: Activity of the three different classes of retinal ganglion cells in dark-adapted retinas evoked with spots of light. In response to their preferential stimulus the activity of the RGCs increases. Adopted from [28].

2.3.2 Spatial integration of visual stimuli: Receptive Fields

Importantly, RGCs modulate their spiking activity in response to changes in light luminance occurring within a limited portion of the visual scene, called the receptive field (RF). The RF of an RGC includes all the inputs from photoreceptors connected to that cell via bipolar cells, horizontal cells, and amacrine cells.

The RGC RFs are approximately circular, and they consist in a centre and a surround region with an antagonistic behaviour: if the preferred stimulus is presented within the RF centre, the RGC steadily increases the firing rate, whereas if the same stimulus is presented in the RF surround the RGC reduce its firing rate.

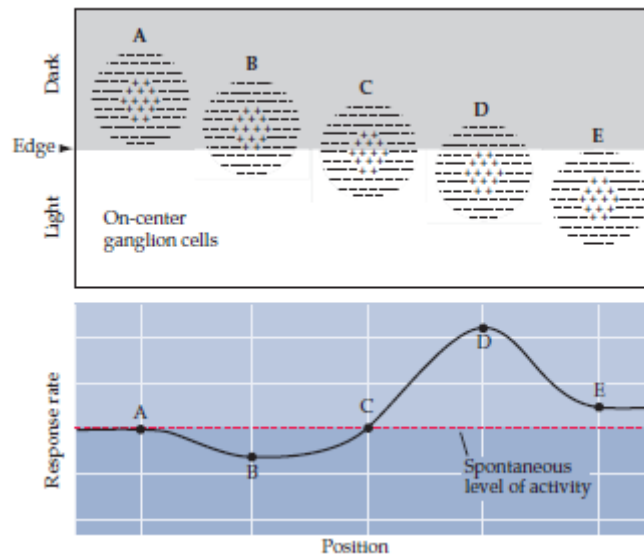


Figure 2.5: Prototypical responses of an ON-RGC to a light-dark curtain image as a function of the relative position between the RF centre and the white edge of the curtain. Depending on the overlap between the RF and the white curtain, the ON-RGC: (A) remains at its baseline activity, (B) is depressed by the inhibitory effect of the surround, (C) returns to its basal activity as the centre excitation balances the surround inhibition, (D) is fully excited as the centre is maximally exposed to the white part, and (E) stabilizes its firing rate to a value higher than (A) since the centre excitation dominates over the surround inhibition. Image adapted from [29]

Figure 2.5 shows the typical response of an ON-RGCs to a light-dark edge image in which the white region increasingly overlaps with its RF. In configuration (A) the overlap between the white area and the RF is zero and it is firing at its basal level of activity as it does not experience any change in light luminance (red dashed line). In configuration (B), the white region overlaps only with the RF surround and thus the RGC firing rate decreases with respect to (A) due to the inhibitory effect of the RF surround. In configuration (C), the preferred stimulus partially overlaps with the RF centre, and the excitatory contribution of the RF centre balance the inhibitory response of the RF surround. In configuration (D), the white curtain covers the RF centre entirely; consequently, the RGC mean firing rate steadily increase towards its maximum value. Finally, in configuration (E), the white stimulus covers the RF completely and the firing rate decreases with respect to (D) because of the additional inhibitory contribution of the RF surround. Note that in configuration (E) the firing rate is still higher than the basal value (A) because the excitatory contribution of the RF centre dominates

over the inhibitory contribution of the RF surround. Finally, the RGCs can also be classified according to the kinetics of their RF response, as transient or sustained. Transient RGCs respond to the stimulus with a brief activity just after a stimulus is presented to the retina; instead in sustained RGCs the response is a continuous ring for all the duration of the stimulus [30].

Therefore, according to what was said before, the classification of functional RGC-types and the estimation of their RF size are essential parameters for investigating the information processing performed by the retinal circuit.

Methods for Receptive Field estimation

The aim of the receptive fields estimation is to understand the relationship between the extent and position of an object appearing in the visual scene in modulating the RGCs spiking train response.

The most common model used to study RGCs RF is the difference of Gaussians (DOG) (Figure 2.6) in which the RF has a shape of two 2D Gaussians [31]. This model assumes that the RGC response is the result of the combination of the center and the surround that, as explained in Section 2.3, respond to contrast stimuli. The model described is easily fit from any of the RF measurements described in the following lines.

All the methods that will be described in this Section rely on a single assumption derived from an oversimplified view of the retinal processing: the RF is not changing over time or in different luminance conditions. However, several adaptation phenomena to light stimuli occur in the retina, thus confirming that its visual information processing dynamically change and optimize its performance in any given condition[32]. Therefore, for the measurement of the RFs it is also essential to consider the stimulation time required to obtain the relevant information. Thus, the stimulation time interval represents a compromise between experimental needs and estimation accuracy.

The advantage and disadvantage of the principal types of visual stimuli adopted for the estimation of RFs are the following:

- **Sparse noise:** spots of light are presented to the retina in random locations(Figure 2.7A). With this method, the RF is defined as the region in which the spot elicits a response [33]. The main advantage of this method is the straightforward interpretation of the RF that allow the identification of the RGCs preferential response (ON, OFF or ON-OFF). A disadvantage of this method is the necessity of many repetitions of visual stimulation, and thus long-lasting experimental phases, to obtain a robust RF quantification and information about the kinetics of the response; on top of this, it also require to consider each cell at a time. Finally, this RF estimation depends on the size and intensity of the spots used for visual stimulation.

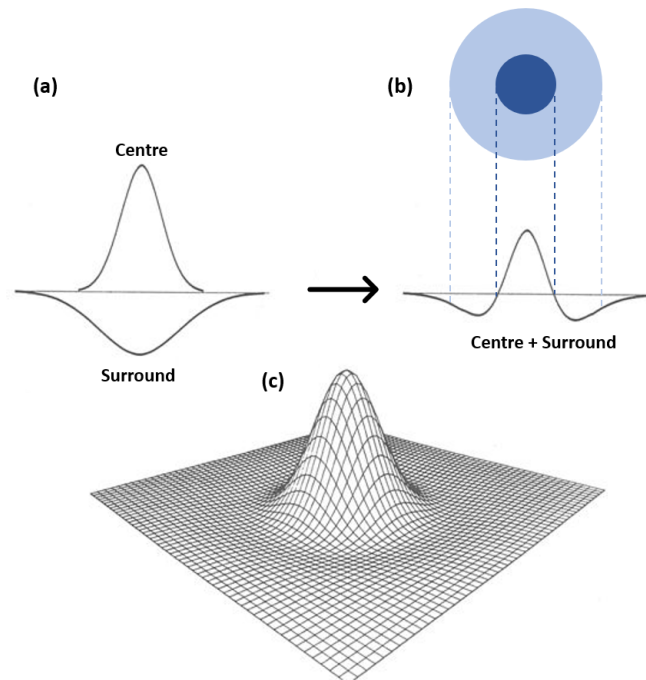


Figure 2.6: The DOG model for RF analysis. (a) The spatial sensitivity of the center and surround mechanism both have a Gaussian profile. (b) The neural response is the result of the linear summation of the two independent mechanisms, the center and the surround (c)

- **Spots of variable sizes:** this method is an improvement of the previous one as in this case a spot of light is presented in the same position for different diameters (Figure 2.7B) centred with the position of each cell. The smallest size of the spot that elicits the maximum response is considered as the dimension of the RF center [34]. Similarly to the sparse noise methodology, also this method relies on a brute-force approach consisting of showing a plethora of stimuli. Further, this procedure implicitly forces the shape of the RFs to equal the one used as probing stimulus (usually a circular spot) and thus can provide hints only on RF size.
- **Drifting gratings:** differently from the other two methods, the estimation of the RF is based on sinusoidal drifting gratings (Figure 2.7C). After the quantification of a retinal ganglion cell sensitivity in responding to gratings of different spatial frequency, the RF extension is estimated by computing the inverse Fourier transform of the spatial sensitivity from the frequency

to the spatial domain [35]. Given that the stimuli used are spatially invariant, i.e. repeat along the movement direction of the grating, this method allows quantifying RFs of several different RGCs simultaneously with a few parallelizable and rapid computations. Thus, this approach is particularly suitable for large-scale multi-electrode array recordings. Another advantage of the drifting gratings method is that the stimulation can be repeated several times in a few tenths of seconds, leading to an effective description of each RGCs response. By presenting gratings moving in different orientations, it is possible to refine the RF estimation and further characterize the orientation and direction selectivity properties of the RGCs. Nevertheless, this method assumes implicitly that the retina encodes static images and moving objects in a similar fashion. Instead, a disadvantage that affects this and the previous methods is that the estimation of the center size depends on the strength of the surround suppression: if the surround suppression is strong, the center size will be underestimated, instead if the surround suppression is weak the size of the center will be overestimated.

- **Spatio-temporal white noise:** this approach is the state-of-the art methodology for the estimation of RFs, especially if concurrently associated to a spike-triggered-averaging (STA) analysis method [14]. A sequences of images consisting in a checker-board with randomly distributed white and black pixels (Figure 2.7D) is presented to the retina to elicit RGCs responses induced by the different arrangement of black and white pixels from one frame to the following. Next, by averaging those stimuli that evoked a response can be estimated the size of the receptive field. The spatio-temporal white noise stimuli with the STA analysis has some limitations. The major one is that is not possible to identify the polarity of the RGCs (ON, OFF or ON-OFF) or come up with kinetic information, besides is necessary to consider that the checker size for a robust RGC response depend on the activation strength of its RF center and surround. Instead the main advantage of this method is that it avoids adaptation to strong or prolonged stimuli and, thus, is well suited to simultaneous measurements from multiple neurons. However, it provide the most accurate description of RF extent at the price of a long-lasting experiment.
- **Filter back-projection:** single bars are flashed to the retina in different positions and with different orientations (Figure 2.7E). After a back projection filtering, a signal processing technique widely used in computerized tomography, is applied to the recording data. Starting from a one-dimensional view of the data, the filter back-projection construct a two-dimensional image [15]:

after each stimulus the data recorded are used to build a map for the RF relative to the position and orientation of the bar. The different maps obtained are then averaged in order to reveal the ridge of increased activity that is the region of the RF. This approach allows the differentiation between ON and OFF RGCs and, for long stimulation periods, it is also possible to extract kinetic information of RGCs, analyse many RGCs simultaneously and, since the stimulus consists in elongated bars, extract information about orientation selectivity. The principal disadvantage of this approach is the projection and reconstruction artifacts.

- **Natural stimuli:** naturalistic images (Figure 2.7F) are also used to study the response of RGCs to more physiological stimuli. In this case, linear analysis methods, like STA, would not provide satisfying results as a consequence of spatial correlation embedded in natural images. Indeed, one of the assumptions of the linear method is the zero correlation between the stimuli [16]. Consequently, although more physiological, this approach further increase the complexity of the problem but, if carefully used, can lead to the identification of possible non-linear interactions between neurons.

Method	ON-OFF separable	Spatial resolution	Kinetics information	Parallelizable	Fast stimulation
Sparse noise	++	–	++	--	++
Spots of variable sizes	++	--	++	--	++
Drifting gratings	--	–	+	+	++
Spatio-temporal white noise	++	++	+	+	--
Filter back-projection	+	–	++	+	–
Natural stimuli	--	–	+	++	--

Table 2.1: Qualitative summary of the pros (+) and cons (–) of the available approaches for receptive field estimation.

The following Chapter reports an overview on the electrophysiology approaches developed in neuroscience to record the bioelectrical activity of neuronal circuits, and in particular retinal circuits, with the goal of investigating their operating principles.

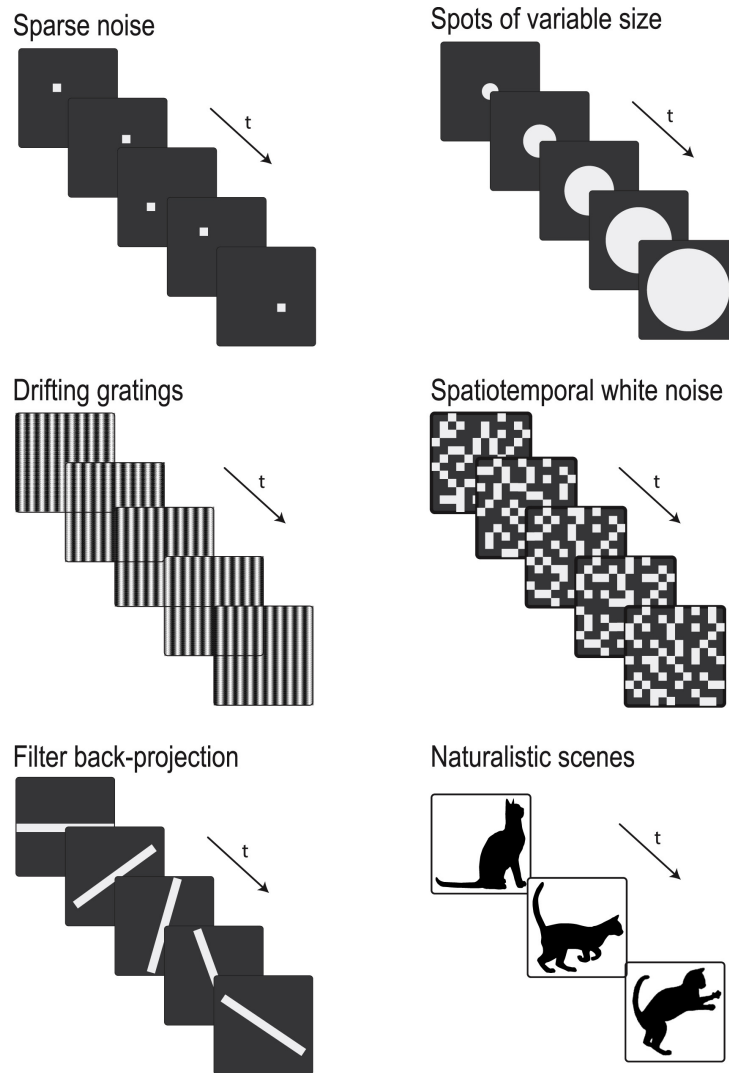


Figure 2.7: Visual stimuli used for RF estimation. Image adapted from [36]

3 Electrophysiology: the study of neuronal bioelectrical activity

Electrophysiology in neuroscience aims at studying the electrical properties of the central and peripheral nervous system. During the last decades, the technological progress promoted the development of increasingly sophisticated and accurate devices and methods to monitor and investigate the bioelectrical activity of single neurons or complex networks in living organisms, *in vivo*, or isolated from their normal biological context, *in vitro*.

The major advantage of *in vivo* studies lies into the possibility to analyse neuronal dynamics truly reflecting the physiology of an intact neuronal circuits in living beings. For this this reason, *in vivo* studies are believed to provide conclusive hints on the nature, mechanism or function of the phenomena under investigation. Nevertheless, the interpretation of results obtained *in vivo* should be carefully evaluated because of a number of factors (for example the inter-animal variability and the intrinsic spontaneous activity), that are inherited by the complexity of the system and are out of the experimentalist control, can lead to misleading conclusions.

Conversely, *in vitro* studies use simplified isolated models of the neuronal network or brain circuit physiology to focus the analysis on a neuronal preparation growing from sketch in a controlled environment and completely isolated from the living organism. Although *in vitro* experiments represent a good starting point for the analysis of a specific neuronal target, they require to perform an essential validation step to ensure that the *in vitro* neuronal networks mimic the salient biochemical and electrophysiological features of the original system.

In between the two mentioned approaches there is the experimentation performed on a tissue dissected from a living being in a controlled environment outside the organism. By performing experiments on a genuine tissue in a controlled environment, this type of neuronal preparation is a compromise between *in vitro* and *in vivo* studies. However, maintaining the viability of tissue and failure in replicating *in vivo* physiology due to isolation (e.g., lack of inputs) represent two major disadvantages.

Method	Pros	Cons
<i>in vivo</i>	- Study neuronal dynamics in living organism	- Invasive - Complex biological variation
<i>ex vivo</i>	- Easily accessible - Intact physiological circuit	- Difficulties in maintaining viability of the dissected tissue - Failure in replicating <i>in vivo</i> physiology due to isolation
<i>in vitro</i>	- Simple set-up - Reproducible - Non-invasive	- Need of essential validation step - Not able to accurately predict the conditions inside a living organism

Table 3.1: Advantages and disadvantages of the three principal approaches in electrophysiological investigations.

The next Section reports an overview of the main methods for recording neuronal bioelectrical activity with their pros and cons. Next, the pre-processing flow of data analysis is described in detail, with a particular focus on the redundant information acquired by high-resolution multi-electrode arrays. Indeed, redundant information can be either useful, as in refining spike-sorting procedures, or harmful, as in providing real-time closed-loop feedbacks. Finally, the section ends with an overview of closed-loop approaches used to highlight their importance in modern neuroscience.

3.1 Monitoring the bioelectrical activity of neuronal tissue

The bioelectrical signals generated by neurons can be monitored through direct or indirect methods. Indirect measurements track second-order effects of neuronal communication and consequently provide a coarse quantification of the activity of many neurons. For example, the functional magnetic resonance imaging (fMRI) does not record neuronal activity directly but provides a measurement of the changes in blood flow and oxygen consumption [37]. Neuroimaging techniques, such as electroencephalography (EEG), magnetoencephalography (MEG) and positron emission tomography (PET) provide low-resolution images of large brain areas and thus are useful in expanding the knowledge derived from the study focused on single neurons at the brain scale by providing snapshots of the entire brain in action. Each pixel in the neuroimaging snapshot, the voxel, represents the average activity of at least 80,000 neurons and 4.5 million synapses. Consequently,

an image of fMRI is unsuitable for identifying and dissecting the micro-circuits involved in a particular task. Likewise, the EEG appears to be a weak technique to investigate the operating principles underlying neuronal computation as it provides an averaged, low-frequency filtered, measure of the electrical activity of over 100,000 neurons limited to the most superficial neuronal layers.

3.1.1 Single neuron measurements

Although neuroimaging techniques are useful for their non-invasiveness and for the possibility to observe the activity of extended neuronal networks, the monitoring of second-order effect of the spiking activity, in general, result in a poor temporal resolution compared to the brain dynamics. Indeed, information processing in the brain is a highly dynamic process occurring on a milliseconds timescale. Thus, to investigate fast-changing dynamics in single neurons, methods based on electrodes are currently the best candidates.

The function of single neurons is often explored by direct measurements of the intracellular voltage changes, with respect to time, across the membrane during action potentials (Figure 3.2). The most traditional intracellular technique used to study a single cell is the patch clamp [38]. It consists in placing on the cellular membrane a thin and hollow capillary electrode (Figure 3.1A) with a diameter of about one micrometer.

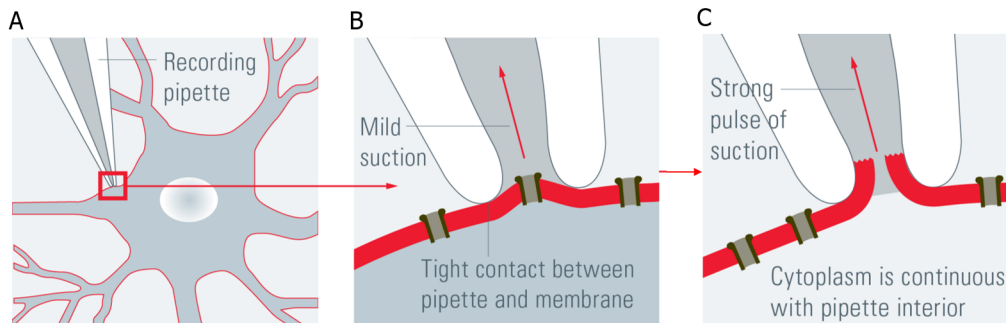


Figure 3.1: Representation of the patch clamp technique. Image adapted from [39]

By applying a slight suction in the hollow capillary, the cell membrane is "sucked" slightly inside the electrode (Figure 3.1B). This creates a "seal" that isolates the analysed portion by the rest of the cell membrane. A further negative pressure determines the break of the cellular membrane (Figure 3.1C) allowing direct contact between the electrode and the intracellular environment. Therefore,

this technique allow to fully record the bioelectrical activity generated by the target neuron including spiking activity and sub-threshold oscillations.

The patch clamp also has some drawbacks: first, its invasiveness as the micro-electrode damage the cell upon perforation, second, the limited amount of neurons that can be simultaneously recorded, due to the bulky instrumentation required. On the other hand, the activity of single-neurons can be explored through extracellular recordings using metal electrodes located in the extracellular environment close to the neuron. In this case two different signals can be observed:

- **Extracellular Action potentials (EAP):** are very fast signals occurring when the membrane potential of a specific axon location rapidly rises and falls. Physiologically, APs frequency can reach up to 200 - 300 Hz and the signals are usually very well localized in space as shown in Figure 3.2A (middle).
- **Local field potentials (LFP):** signal generated by the electric current produced by a group of dendritic synapses within a small volume of nervous tissue. The voltage is produced by the sum of the synaptic current flowing through the local extracellular space. The LFP are signals mostly slower than the APs and present typically low frequencies (0.1 - 100 Hz). Differently from APs, the LFPs are very spatially broad signals.

Extracellular recordings are used specifically to detect whether or not an action potential (spike) has occurred in a specific timestamp, with no particular consideration to the waveform in case of the single neuron recordings, because spike waveforms recorded by extracellular recording devices vary in shape and amplitude between neurons due to morphological and electrical features of each neuron and position of the recording electrode. Instead for multiple recordings the waveform is needed in order to perform the spike sorting (see Section 3.1.3).

The big advantage of the extracellular recording is the possibility to monitor the neurons activity for days or months without inflicting any mechanical damage to the neuron membrane. But this characteristic affects the signal amplitude because compared with that of the intracellular recording, the extracellular one is lower (see the different scales in Figure 3.2B). Moreover with the extracellular recordings the sub-threshold events can not be observed.

While the intracellular recording is an essential tool for investigating synaptic communication between pairs of neurons, the latter deficiency prevent from the investigation of information processing in a dense cellular network, such as a neuronal culture, in which each cell contact, through the synapses, hundreds of other cells.

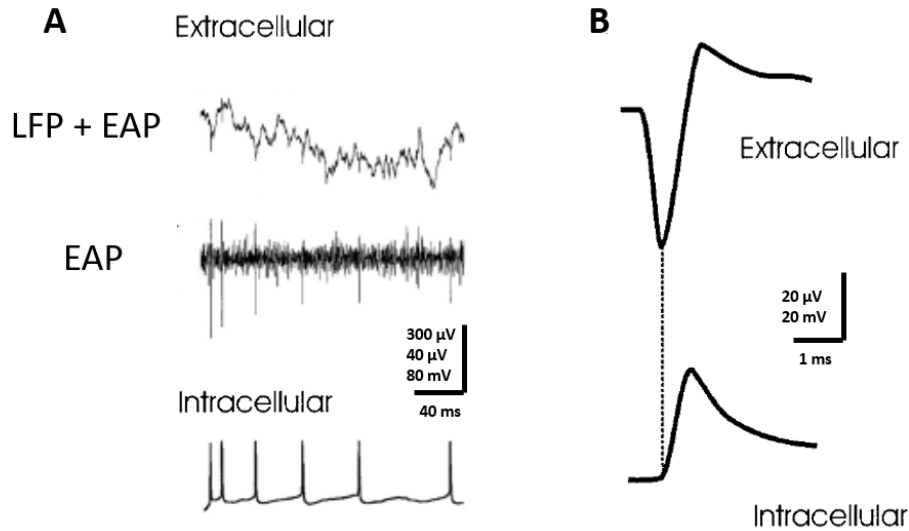


Figure 3.2: Signals for simultaneous extracellular and intracellular recordings from CA1 pyramidal cells. (A) *Top*: wideband extracellular trace. *Middle*: high-pass filtered extracellular trace. *Bottom*: intracellular trace showing action potentials. (B) Simple waveform of a spike recorded extracellularly and intracellularly. Note the different amplitude scale of the signals. Adapted from [40]

3.1.2 From single neurons to networks

As for single-neuron measurements also neural networks can be studied with electrodes, in particular the progress of microtechnology has allowed the development of Micro-Electrode Arrays (MEAs), i.e. devices that provide an extracellular electrophysiological measure of neuronal networks activity through high temporal resolution recordings over multiple electrodes simultaneously [41], [42].

MEAs development starts in the 1970s and progressed with the advances in microelectronics and microfabrication processes with the aim of simultaneously acquiring millisecond temporal resolution voltage traces of the electrical activity of the largest number of neurons possible.

The first devices realized were passive electrode arrays, embedded in glass or silicon substrates and became commercially available in 90s [43]. In detail, each microelectrode on the array is passively connected through metal wiring (Figure 3.3A) to an off-chip electronic circuit that performs signal conditioning, multiplexing and analog-to-digital conversion. The broad use of these devices originates from their simple, yet powerful, design that allows the simultaneous recording of a few tenths of electrodes in various neuronal preparations, including neuronal cultures [44] and ex-vivo tissue [45]. However, the physical space consumed in electrode wirings to

INTRACELLULAR RECORDINGS	EXTRACELLULAR RECORDINGS
Sharp and patch electrodes	Substrate-integrated MEAs
Individual neurons: how they transmit electrical information, communicate and compute subthreshold synaptic inputs	Neuronal networks: possibility to monitor long-term electrophysiological correlates of plasticity and learning
Limited duration of recording sessions (mechanical and biophysical instabilities)	Days/months without inflicting mechanical damage to the neuron membrane
Current signals from which it is possible to obtain action potential ($\Delta V \sim 100$ mV)	Voltage signals in the range 0.01 mV – 1 mV
Very good electrical coupling with the cell that results in a low noise recording	High noise level: ~ 10 μV
Direct measure: no distortion of the readout over time	Electrical signals are largely attenuated and temporally filtered

Table 3.2: Comparison between extracellular and intracellular recordings.

off-chip electronics preclude the scaling up of the number of electrodes because of the limited area available on-chip. To improve passive electrode arrays, MEAs developments focused on three principal directions:

spatial extent: increase the number of neurons observed by incrementing the number of electrodes to track the activity of entire neuronal networks;

noise reduction: closing the distance between the sensing electrode and the amplifier contributes to the overall noise reduction because the coupling among adjacent metal lines is reduced and the external noise sources picked up by long metal lines acting as antennas are reduced;

spatial density: incrementing the density of electrodes to match the neuronal density, possibly providing a one to one electrode-neuron mapping or sub-cellular details.

The technological solution introduced to tackle these issues was the integration of electronic circuits (e.g. amplifiers, ADC converters) right below the plane of electrodes [5]. Performing most of the pre-processing operations directly on-chip made possible to significantly scale-up both the electrode density and the spatial

sampling extent with an acceptable level of noise. This active design of electrodes paved the way to the next-generation MEAs that consists of miniaturized implantable recording arrays that satisfy the constraints of chronic behavioural studies [46].

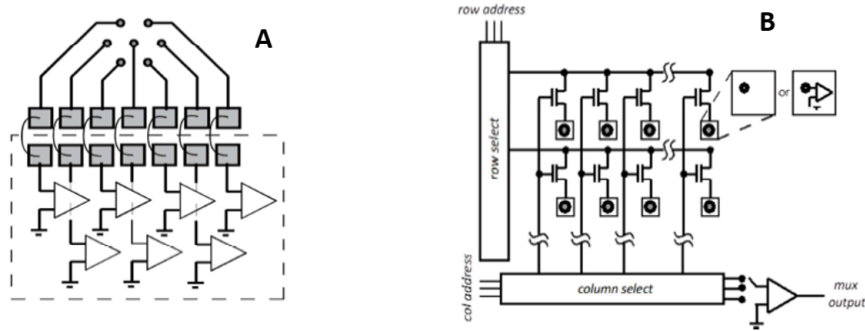


Figure 3.3: Examples and concepts of passive and active electrode arrays. (A) In passive MEAs, electrodes are individually wired to an external signal amplifier. These devices are realized using MEMs or NEMs micro-/nano-structuring processes. (B) Active MEAs integrate the electronics on-chip multiplexing the signal through contact pads [47]. These new generation of monolithic devices are realized using CMOS technology.

In detail, to realize large and dense matrix composed of several thousands of electrodes, active circuits have been implemented exploiting standard complementary metal oxide semiconductor (CMOS) technologies [47], [48]. The CMOS technology allows realizing active electrode-pixels that integrate into a few square micrometers the neural-electronic interface, i.e. the electrode and, just underneath each electrode site, the signal conditioning circuits, i.e. the amplifiers. Additional amplification stages, time-division multiplexing and high-speed addressing circuits are provided on-chip to fully exploit the limited electrode wiring of passive arrays (Figure 3.3). Instead of outputting a passive electrical shortcut, these devices transmit an already digitized and multiplexed signal, allowing to design MEAs consisting of thousands of closely spaced microelectrodes. With these devices, the bioelectrical activity of extended brain tissues can be monitored and investigated through extracellular recordings. The first platform based on CMOS technology for extracellular recordings [5] has 4096 recording sites arranged in a 64x64 matrix. This device is described in details in Annex I. Besides the technological challenge

to further increase the spatial sampling, the development of computational tools that can handle, manage and make sense of high-density MEA (HD-MEA) recordings remain still a challenge due to the huge computational cost required for the analysis of thousands of simultaneously recorded units.

Another approach for the monitoring of the activity of neural networks is represented by the calcium imaging technique [49]. Among ion species, the intracellular concentration of calcium ions (Ca^{2+}) plays a relevant role in establishing the membrane potential of the neurons. Thanks to fluorescent molecules that bind Ca^{2+} , it is possible to see the activity of single neurons as an increase and decrease of the fluorescent signal. In contrast to the patch clamp technique, with calcium imaging, it is possible to simultaneously analyse the activity of thousands of single-neurons. However, the time-course of calcium signals (100 ms) is two orders of magnitudes slower than the spike generation (1 ms) and thus, calcium imaging is not sensitive neither to single spikes nor sub-threshold activity, due to signal to a low signal-to-noise ratio. Nevertheless, the great advantage of the calcium imaging, is that it can be used *in vivo* on awake and living animals, allowing to correlate the activation (or the inhibition) of a brain region with the behavior that follows.

3.1.3 Identification of single units in extracellular recordings

Opposite to patch clamp or intracellular recordings where one electrode is sensing the activity of one neuron because it is placed in direct contact with the neuron, in extracellular recordings, the electrodes are equally spatially distributed in the extracellular environment. Each extracellular electrode might be sensitive to different neurons located in its surrounding area, hence is essential to associate each spike detected to the originating neuron. Although action potential, or spikes, are ascribable to all or none digital phenomena, each neuron gives rise to a slightly different time-course of the electrical signal depending on its size or shape. Further, the recorded waveform is susceptible to modulations due to the relative distance between the neuron and the electrode and the conductive properties of the electrode-neuron interface. Conventional algorithms take advantage of this heterogeneity to identify single-neuron spiking activity by grouping together similar action potentials. This is often achieved by comparing the spike amplitude, or more accurately, by considering the whole waveform through data-reduction techniques as the principal component analysis or the Wavelet transform.

The process of assigning each action potential to the originating neuron is called *spike sorting* and is schematically represented in Figure 3.4. The ultimate goal in improving spike sorting techniques is to implement a fully automatic procedure

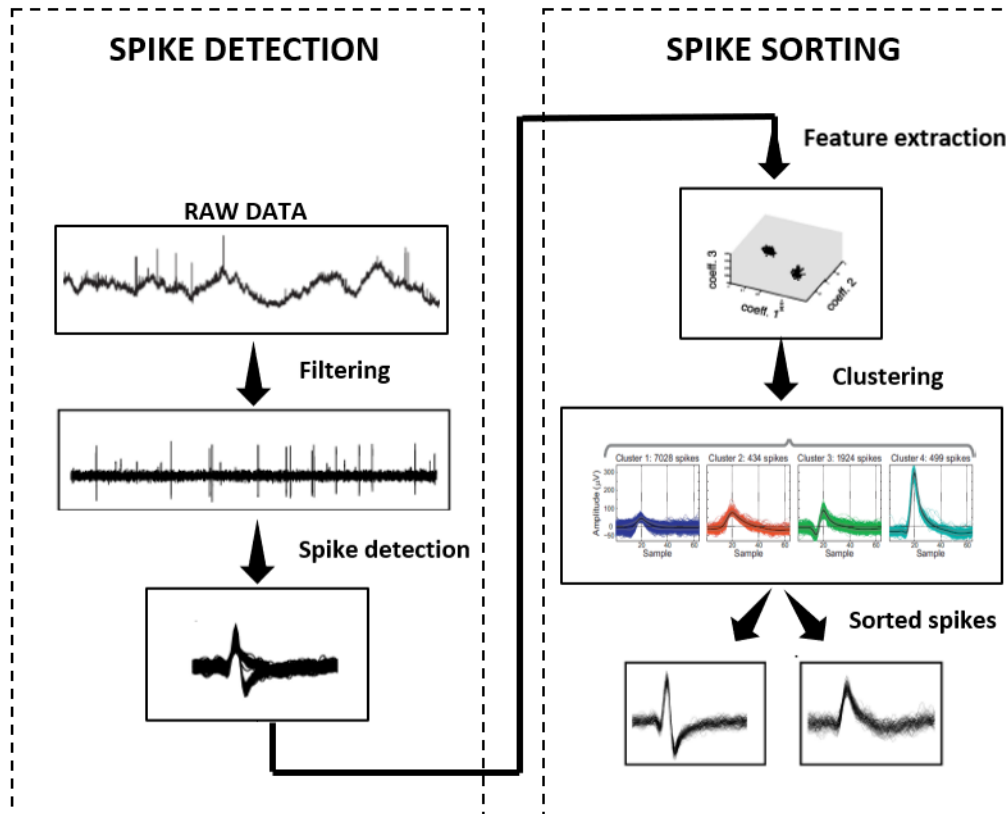


Figure 3.4: Schematic pipeline for spike sorting. Starting from the recorded raw data, the signal is bandpass filtered to ease the spike detection phase, usually based on an amplitude threshold. After spike detection, the relevant features of the spike (waveform, position, etc..) are extracted, for a dimensionality reduction step. Finally, a clustering algorithm based on the reduced information associate each spike to a single unit. Adapted from [50]

capable of accurately discriminating the contribution of single neurons in a signal consisting of superimposed spiking activity of several units. As shown in Figure 3.4, the spike sorting pipeline and consist of the following main steps:

- bandpass filtering of the raw signal. The filtering step is needed to increment the signal-to-noise ratio and consequently lower false-positive spike detection rates. Typically hardware acquisition systems include a first analog causal infinite impulse response (IIR) bandpass filter (e.g. 300 Hz to 3400 Hz [13]) due to their easy implementation. For a more accurate signal filtering is necessary a finite impulse response (FIR) filter that avoids a signal distortion keeping the shape of the spike unchanged. In order to simplify the next steps,

a second more restrictive digital bandpass filtering is applied by software.

- detection of spikes in the filtered signal. The spike waveform has a biphasic deflection, hence, the spike detection is usually based on a threshold crossing approach paired with acceptance criteria as the presence of a biphasic waveform [51]. The threshold value depends on the noise level that is estimated in a time interval that does not contain spikes to prevent from the detection of waveforms whose amplitude is similar to the noise level. Because spikes are sharp and transient variations of the extracellular potential, the threshold is often based on the standard deviation of the filtered acquired signal. However an estimation based on the median absolute deviation of the filtered signal has been proven to provide more robust quantifications [50].
- data reduction to identify relevant features of the spike waveforms. Although computational demanding, the extraction of relevant features simplifies and speed up the subsequent clustering step by reducing the dimensionality of the problem. The most widely used approach is the principal component analysis (PCA) that provide a new reference system that maximizes the variance of the data along its dimensions. In the new reference, only a few components are retained for further analysis significantly reducing the dimensionality of data. Other methods include the independent component analysis (ICA) [52] or the wavelet decomposition [53].
- clustering algorithm to discriminate single spiking units. With the advent of the high-resolution recordings, the spike sorting requires a high computational cost due to the iteration of the mentioned procedure over thousands of electrodes. However, in high-density recordings, the clustering step of spike sorting algorithms can take advantage of the redundant information recorded by neighbouring channels to further refine the classification. The latter intuition was implemented on HD-MEAs recordings following two main ways: creating spike templates and sorting through a template matching procedure or reducing the dimensionality of the data and applying fast clustering methods. The clustering algorithms are usually affected by the following issues:
 - in extracellular recordings the shape and the amplitude of the spikes may change during bursting;
 - synchronous and spatially-clustered events produces overlapped waveforms;
 - electrodes are subjected to relative movements between the neuron and the electrode position;

- duplicated spikes over neighbouring channels lead to misclassification;
- the number of recorded neurons is a priori unknown.

Many spike sorting methods exploit Gaussian Mixture Models (GMMs) for the fitting and regularization of the data [54], and Bayesian classifiers for the subsequent clustering step [55]. However, these two methods do not perform well in case of large-scale recordings because of their demanding computational cost.

All the spike sorting techniques described are adapted for recordings obtained with traditional MEAs as they rely only on the information provided by a single electrode voltage trace. However, in high-density recordings, the same unit can be detected from different neighbouring channels, and thus, spatial redundancy can be exploited for spike sorting. In particular, in [56] is presented an automated spike sorting method for large-scale recordings that exploit this redundancy to estimate the spatial locations of spikes in the space. The combination of the estimated spike position and the features of spike waveforms determine an efficient and low-dimensional representation for clustering the detected spikes. It has to be noted that spike sorting approaches require the acquisition of several hundreds of seconds of spiking activity to accurately discriminate between different units and are too computationally demanding to run in real-time.

In real-time applications, it is not trivial to exploit the redundant information acquired by adjacent electrodes given the hardware constraints but it rather leads to waste of computational resources in analysing duplicate spike trains, as no spike sorting is performed. As a consequence, to speed up the on-board analysis and fully leverage the limited amount of hardware resources, it is necessary to detect and clean spike trains from duplicate spiking activities.

A robust approach for duplicate spikes removal would consider only the largest amplitude spikes recorded within a fixed radius, thus blanking all the waveforms acquired in adjacent electrodes with a smaller peak-to-peak amplitude. This approach is suitable for the separation of near-synchronous spikes which occurs in a given spatial area of the MEA. However this method requires to analyse the entire waveform. Indeed, small temporal jittering, spatial decay of the signal and different noise levels should be carefully taken into account.

All these task are highly time and memory consuming for real time applications, consequently, an alternative approach for the removal of the duplicate spikes is to perform the identification of the same event after the spike detection and to consider only the timestamps of the spikes. In this way the waveform of the spike is not anymore taken into consideration.

In the following part, the principles of the real-time applications for closed-loop architectures are described with a focus on their utility in modern neuroscience.

3.2 Investigating the input/output properties of neural networks

The central nervous system (CNS) of humans and animals has to face daily with an uninterrupted and rapidly changing stream of sensory information. Moreover most of the neural networks of the sensory organs are perturbed by the external environment through mechanical, optical or electrical stimulations.

In order to understand the relationship between the input (stimulation) and the output (spikes) of the nervous system, neuroscientists have developed sophisticated open-loop approaches to perturb single neurons or neural networks and analyse their behavioural response to the external stimulations. These strategies consists in the application of a stimulation that does not change in response to any continuous measurement of the level of neural activity that is generated.

Open-loop strategies can work well for systems for which the model of the response is known and the disturbances are measured. However, since the neuronal computation consists of the integration of thousands of synaptic signals on the dendrites into a spiking pattern in the axon, the responses of individual neurons to ongoing input are highly variable. Nevertheless developing a suitable simplified model of the system of interest as an open-loop system is often a first step. However the fully characterization of the neuronal input–output relationships is practically intractable due to the non-linearity of the system and the cumulative effect of neural processes spanning a wide range of time-scales.

In this perspective the research in neuroscience became involved in the development of closed-loop systems that exploits the real-time investigation of the neural activity after specific stimulation.

3.3 Closing the loop: real-time interaction with neuronal networks

The nervous system is based on feedback/closed-loop controls ranging from ion channels regulation to neuronal networks. Thus, brain signals reflect controlling behaviour of the brain as a result of the integration of the received information from sensory organs. Recent innovations in analog electronics, real-time computing and digital signal processing allow the analysis of the brain system in closed-loop architectures, thus stimulating the neurons according to their current state. In Figure 3.5 is shown a typical configuration of a closed-loop system.

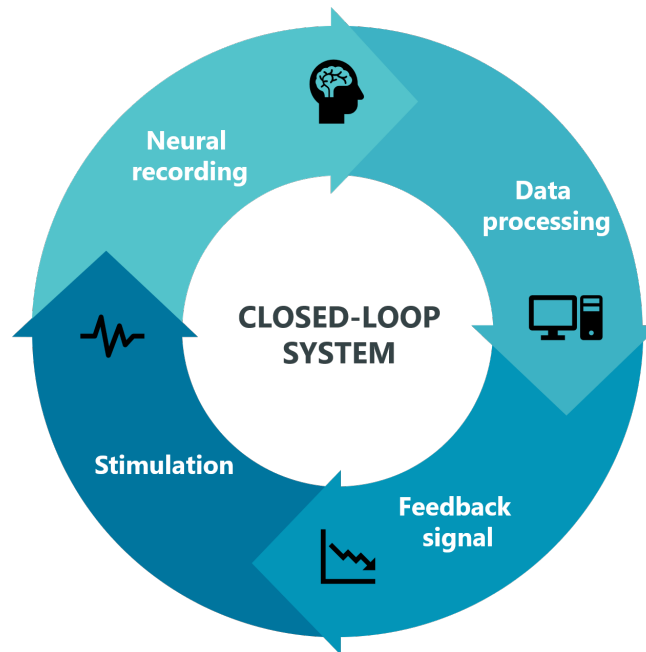


Figure 3.5: Schematic representation of a close-loop approach in neuroscience: according to the neural activity recorded, a processing unit will extract in real-time the most important features of the signal in order to take the decision for the next stimulation.

3.3.1 Closed-loop architectures in brain machine interfaces

The closed-loop approach is widely used in brain-computer interfaces (BCI) [57]. A typical BCI system allows an electronic (e.g. computer) or electromechanical device (e.g. a mechanized wheelchair) to be controlled by voluntary modulation of the user's cerebral activity. It is, therefore, necessary to have a device dedicated to acquire the brain activity in real-time and a device that basing on the information acquired, give rise to a pre-defined operation (e.g. provide a physical feedback).

Closed-loop architectures are also used in neuroprosthetics to mimic the processing of sensory information and restore lost functions trough bidirectional interfaces between the brain and an external device (e.g. a robotic arm or an augmented reality visor). This kind of bi-directional communication of a machine with brain tissue allows us to study in detail the coding and decoding of information processing performed by neurons in complex neural networks.

A pioneering example of this methodology was achieved by interfacing a mobile robot, as an external effector, with primary neuron cultures grown on microelectrode arrays. A closed-loop system between the neuronal network and the robot

[58] was established by a two-way pathway of communication: the proximity sensors of the robot provide information on obstacles to the neuronal culture through a localized electrical stimulation; on the other hand, the monitoring of the activity of the neuronal culture via conventional MEAs control the movements of the robot. By moving the robot through the obstacles of an arena this closed loop system allows to study how the neuronal network learns to avoid collisions as a result of the induced functional and structural synaptic plasticity. Indeed, for different training tests, the electrical stimulations determined by the robot proximity sensors progressively modified the communication pathways in the neuronal cultures and eventually lead to long-term changes in the network connectivity. Remarkably, the resulting network was shown to improve the motor behaviour of the robot indicating that the activity of simple and isolated neuronal networks is capable of learning a relatively complex task if stimulated appropriately.

Taking advantage of the real-time processing of a large stream of neural data acquired with state-of-the-art microelectronics fabrication, as microprocessors and field-programmable gate arrays (FPGAs), neuroscientists have developed more sophisticated approaches for the closed-loop experiments such as motor BCIs, assistive devices, neuromodulatory systems, and other devices with an interface into a subject's nervous system.

Although closed-loop systems have been demonstrated experimentally there are significant limits on our ability to understand the brain activity, and consequently develop control policies for the feedback control. In addition, the majority of the neuroprosthetic systems have been developed using animal models and this require an appropriate method to move these systems in human subjects.

4 Data processing

This section reports in detail the steps required for the extraction of relevant information from the spike trains recorded with the HD-MEAs. As reported in Section 3.1.3, these spike trains may include redundant information as a consequence of the tight spacing between electrodes. Thus, identifying the similarities between spike trains of neighbouring channels at the single frame resolution is essential to avoid biases and duplicate results in the subsequent analysis. After the detection of clusters of Spatially Correlated Electrodes (SCE) with a cross-correlation function, the algorithm selects the representative channel (the one with the highest number of spikes recorded) and exclude the remaining from the subsequent analysis. Subsequently, the identified units are classified, according to their response to a stimulation protocol based on black and white flashes, in ON or OFF RGCs.

To validate the proposed approach, I fist implemented an algorithm that generates synthetic spike trains according to a pre-determined probability of firing. Subsequently, in experimental sessions, the retinal spontaneous activity was collected by stimulating the photoreceptors with an isoluminant gray full-field stimulus (0.11 cd/m²), which represent a steady state basal condition in retinal experiments.

Finally, an algorithm for the RF estimation based on a white-black curtain image whose white edge spans the RF from left to right and vice versa the visual field has been tested.

For simplicity, all the results presented here were obtained by running the algorithms in a closed-loop fashion on already acquired data, i.e., in off-line configuration. The results were further cross-checked by a parallel MATLAB implementation of the same analytical tools.

Acquisition and stimulation device

All the algorithms were implemented and tested in MATLAB for fast prototyping and then translated in C for real application use on the Zedboard, which is the hardware platform for closed-loop investigation used in this work. This device consists of an acquisition and processing platform for closed-loop experiments: the main core is a Xilinx Zynq device with two ARM cores and an FPGA-based

processing platform [13]. This system allows to exploit the potentials of large-scale recording obtained with commercially available CMOS-based MEAs featuring 4096 electrodes [47] and an external optical stimulator. This system process the stream of data to provide the timings of the retinal ganglion cells spiking activity within a maximum latency of 1.86 ms and its detailed description is reported in Annex A.

4.1 Detection of sub-millisecond correlated spiking activities

The cross correlation of two simultaneously recorded spike trains sp_1 and sp_2 quantify their overlap as a function of an offset added to one of the two time series and can be visualized in a correlogram.

Computing the cross-correlation requires, in general, a binned signal. Thus, usually, this measure is applied to the mean firing rates, i.e. average number of spikes occurring in a binned time-interval of the recording, to identify neurons whose spiking activity is similar over the time-scale induced by the given bin size.

Here, by reducing the bin size to the minimum, I used the very same method to measure how similar are two spike trains at the single frame resolution. However, binning thousands of spike trains of long-lasting experiments at single frame resolution is not a feasible task for a real-time application.

However, for all or none signals as the spike trains, it is possible to compute the correlogram by quantifying all the possible pairwise differences between the timestamps of the two spike trains, see Figure 4.1. Next, the cross-correlation is quantified by histogramming these pairwise timing differences. In the correlogram the zero bin indicates how often the two cells fired at the same time, and the positive/negative values represent the various time intervals that one cell fired before/after the other cell. Although this approach is more suitable for our needs it still lead to a quadratic increase in the computational cost as a function of the number of spikes and provide more information than the one required in this work.

Thus, following the previous algorithm, I implemented a lightweight cross-correlation function, reported in Listing 4.1, that is able to detect sub-millisecond correlated spike-trains for closed-loop implementation. The smart implementation proposed, indeed, requires a maximum number of operations that depends only on the number of spikes, rather than the number of bins, and that is bounded by the sum of the number of spikes in each of the two spike trains. To further decrease the overall execution time of the algorithm the analysis is performed only on Active Channels (AE), i.e. channels that are recording more than 0.5 spikes/second.

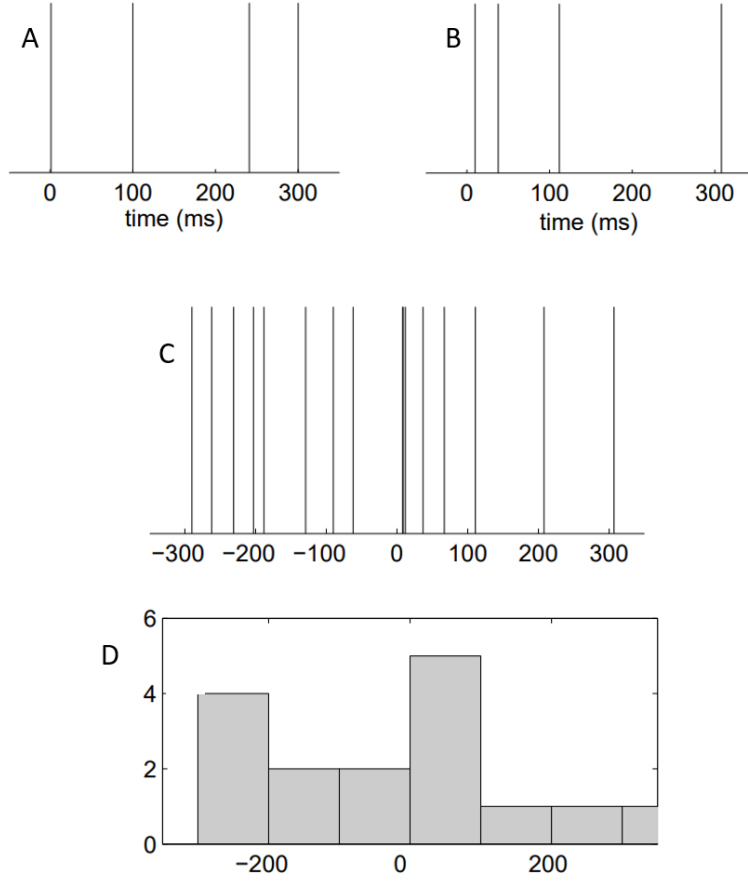


Figure 4.1: Example of the correlogram construction. (A), (B) Two spike trains each with 4 spikes. (C) Position of all the positive and negative time differences between the two spike trains. (D) Histogram of (C), which is the conventional correlogram with bin size of 100 ms. Adapted from [59].

Considering two spike trains sp_1, sp_2 with respectively N_1 and N_2 number of spikes, I introduced a similarity index S , which quantifies in a 0-1 scale how much a spike train is contained into another one, as follows:

$$S(sp_1, sp_2) = \frac{\sum_{i,j}^{N_1, N_2} \delta_{tol}(sp_{1,i}, sp_{2,j})}{\min(N_1, N_2)} \quad (4.1)$$

where δ_{tol} is an indicator function defined as:

$$\delta_{tol}(sp_{1,i}, sp_{2,j}) = \begin{cases} 1, & |sp_{1,i}, sp_{2,j}| \leq 0 \\ 0, & |sp_{1,i}, sp_{2,j}| > 0 \end{cases} \quad (4.2)$$

the parameter *tol* accounts for small jittering in the detection of the spiking activity among different channels and in this work it corresponded to the sampling time-period of the whole-array (0.14 ms).

S is calculated between each AE and each of its corresponding eight neighbouring active electrodes (nAE). Instead, for the channels located at the border of the HD-MEA, the similarity index is set to zero. All the values are stored in a 4096x8 similarity matrix for the subsequent clustering procedure.

Listing 4.1: Cross-correlation algorithm

```
1 for each AE
2 {
3     for each nAE
4     {
5         while i < N1 & j < N2
6         {
7             if (|sp1(i) – sp2(j)| < tol)
8             {
9                 count ++ % count is the number of coincident spikes
10                i ++
11                j ++
12            }
13            else
14            {
15                if (sp1(i) > sp2(j)) { j ++ }
16                else { i ++ }
17            }
18        }
19        if (N1 < N2) { min = N1 }
20        else { min = N2 }
21        return count/min
22    }
23 }
```

4.2 Clustering of redundant spiking activity

As reported in Section 3.1.3, in HD-MEAs neighbouring channels can record the activity of the same neuron. To merge together the electrodes that are recording the same information I identified clusters of electrodes that jointly exhibited high correlation values. The clusters were formed by electrodes that fulfilled the following criteria:

Global similarity: defines the electrodes whose similarity index exceeds 40%. The other channels were discarded as shown in Figure 4.2A.

$$G_{th} : S_{ch1,ch2} > 0.4 \quad (4.3)$$

This threshold prevent from merging weakly correlated electrodes and provide a quick selection criterion of potential candidate electrodes.

Local similarity: is calculated by the following equation:

$$LT_{ch} = \bar{S} + k \cdot \sigma_S \quad (4.4)$$

where \bar{S} and σ_S are respectively the mean value and the standard deviation of the similarity indexes in each row of the similarity matrix, i.e. for each channel, and k is a parameter that defines the restrictiveness of the clustering. Here is set to 1.

Two electrodes A and B were clustered together if their similarity index $S_{A,B}$ exceeded both the local thresholds LT_A and LT_B (Figure 4.2B). This step aims at removing electrode pairs, which, although being similar, can be assigned to a more relevant cluster.

Next, if A was already a member of a cluster, then B was assigned to its cluster (similarly with B). Non-clustered electrodes were considered as a single cluster. Finally, to assign a unique label to all electrode members of a cluster, for each cluster is defined a leader electrode (LE) as the electrode having with the highest firing rate Figure 4.2D. The results were stored in a 4096x1 array, initialized at a non-significant value, were only in correspondence of the LEs and the single clusters of AEs the value was set at the index of each channel.

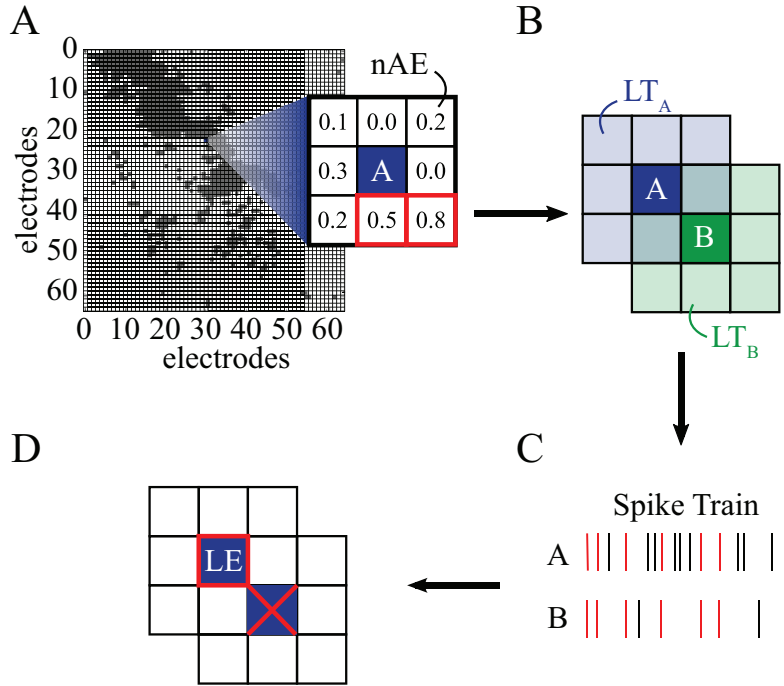


Figure 4.2: Clustering step. (A) HD-MEA active electrodes (black) highlighting the effective coupling of an exemplary retina. Quantification of similarity between electrode A and its neighbouring electrodes (nAE) reveals two electrodes exceeding the threshold of 0.4 (red boxes). (B) Mean plus standard deviation of the nAEs similarity defines the local threshold (LT) for clustering (blue and green shaded region for A and B respectively). (C) Exemplary spike trains of two clustered electrodes with coincident spikes marked in red. The highest firing member of the cluster is selected as leader electrode (LE) and cluster members are removed (D).

Closing the loop: stopping criterion for clustering

By exploiting the close-loop configuration, the similarity matrix and the LEs were updated incrementally every 20 seconds of recording. In this way is possible to save time and memory estimating the amount of data needed in order to achieve a stable configuration of clustered channels.

For each iteration, the algorithm computes the incremental variation between the current and the previous cluster as:

$$\delta_{switch}(k) = \frac{\sum_i \delta(id_i(k), id_i(k-1))}{N} \times 100 \quad (4.5)$$

where δ is the Kronecker delta function, $id_i(k)$ is the label assigned by the clustering procedure to the i -th electrode at the k -th iteration and N is the number of AEs. The clustering algorithm automatically stops once the variation between three successive interactions is below 0.5%, i.e., mismatch of less than 10 electrodes in the worst-case scenario.

4.3 Generation of simulated spiking activity

To test the performances of the cross-correlation function in retrieving and identifying sets of spatially correlated adjacent electrodes (SCE), I implemented the following method for generating simulated spiking activities in which correlations among adjacent electrodes has been artificially imposed.

For each of the 4096 channels, a train of spikes has been sampled according to a probability of observing a spike in a time interval of one second, p_{spike} , that is comparable to the physiological firing rate of a retinal ganglion cell of about 0.5 spikes/second. Then, I created a set of 10 template SCE configurations mimicking the possible spatial organizations of electrodes exhibiting coincident spiking activities that are likely to occur in real experiments, see Figure 4.3. Next, in a random set of candidate electrodes, I imposed correlations in spiking activity between the candidate electrode and its neighbours according to one of the template shapes. The correlations were induced by using two functions that add or remove spikes between pairs of electrodes respectively, according to two following probabilities:

- p_{add} : the probability to add a spike in the two spike trains in the same frame position;
- p_{remove} : the probability to remove a non-correlated spike, i.e. a spike occurring in only one of the two spike trains.

To explore the parameter space, the reconstruction of SCE has been iteratively tested on each possible pair of p_{add} , p_{remove} and k , the parameter that defines the local threshold described in the previous paragraph, see Eq. 4.4. The parameters p_{add} and p_{remove} ranged between 0 and 1 with steps of 0.2 instead k ranged between 0.4 and 1.2 with steps of 0.2.

To quantify the goodness in retrieving the imposed correlations, for each tested condition, the algorithm automatically computed the accuracy, an index that quantify whether the reconstructed SCE actually correspond to the imposed one or not, that is defined as follows:

$$accuracy = \frac{TP}{N_{tot}} \quad (4.6)$$

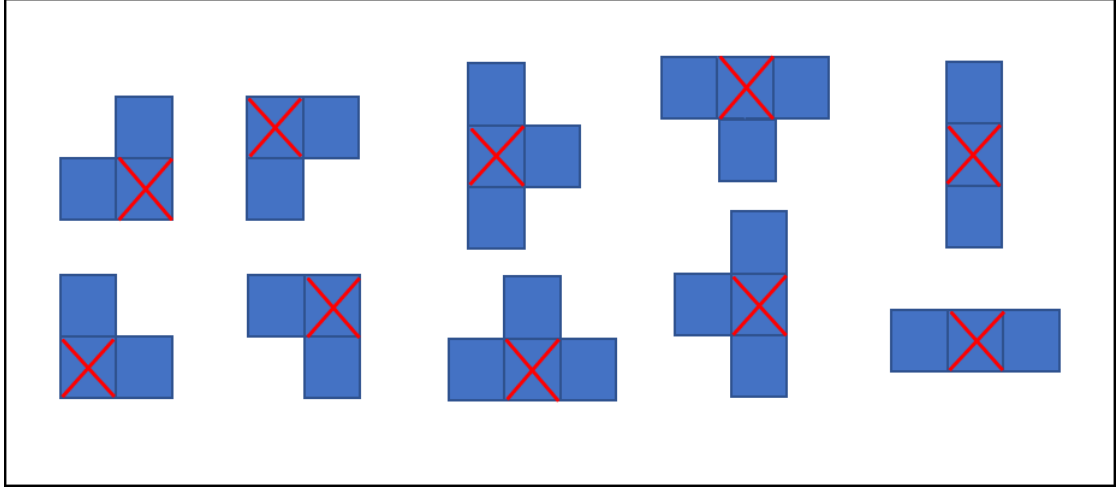


Figure 4.3: 10 sample configuration of simulated correlation between neighbouring channels. The red cross indicates the candidate electrode to correlate with its neighbours.

where TP is the number of correct configuration reconstructed and N_{tot} is the total number of the configuration of correlations imposed.

4.4 Preferential response of the identified units

The next step of the algorithm is the classification of the identified units according their preferential response to white and black full-field flashes. The closed-loop algorithm automatically starts a visual stimulation protocol designed for assigning the previously identified leader electrodes to an ON or OFF RGCs sub-type.

The stimulation protocol consists white and black full-field flashes at maximum contrast (0-0.22 cd/m²) and after each period of stimulation the spiking activity of each unit identified in the previous step is analysed. To do so, the i -th LE that presents an increase (decrease) in the firing activity with respect to the previously recorded basal spiking activity in response to a white (black) flash is classified C_i as "1"("0"):

$$C_i = \begin{cases} 1, & MFR_{i,w} > MFR_{i,g} \wedge MFR_{i,b} < MFR_{i,g} \\ 0, & MFR_{i,w} < MFR_{i,g} \wedge MFR_{i,b} > MFR_{i,g} \end{cases} \quad (4.7)$$

where $MFR_{i,w}$, $MFR_{i,b}$ and $MFR_{i,g}$ are respectively the mean firing rate of

the i -th electrode in response to a white, black and gray isoluminant (basal) visual stimulus. The implementation of the mentioned criterion is reported in Listing 4.2.

Stopping criterion for ON/OFF classification

To refine the classification of ON and OFF units, the algorithm iteratively projects additional white and black stimulation cycles, up to a maximum of NUM_STIM flashes (Listing 4.2), and updates the LEs classification according to the overall spike responses collected up to the current step. This process iterates until the number of LEs transitions occurring between the previous and the current classification, defined as:

$$\delta_{switch}(k) = \frac{\sum_i |C_i(k) - C_i(k-1)|}{N} \times 100 \quad (4.8)$$

constantly remains below 3% for at least three consecutive iterations. Then, the last cell-type classification is considered as the most reliable.

Listing 4.2: Close-loop algorithm for RGCs classification

```

1 while (stim < NUM_STIM & flag = 0)
2 {
3     C1 = C2 % save previous configuration
4     for each identified unit
5     {
6         if (MFR_b < MFR_g && MFR_w > MFR_g)
7         {
8             C1(i) = 1
9         }
10        if (MFR_b > MFR_g && MFR_w < MFR_g)
11        {
12            C1(i) = 0
13        }
14        switch = |C1(i)-C2(i)|
15        if (switch != 0) { counter++ }
16    }
17    if (counter <= 3) { flag = 1 }
18 }
```

4.5 Estimation of RGCs RF

The final step consists in the estimation of the RF of each unit identified previously. To do so the size of single-channel receptive field (cRF) is estimated taking inspiration from the paradigm presented in Figure 2.5. A white-black curtain image whose white edge spans the RF from left to right and vice-versa induce a modulation in the firing activity of retinal ganglion cells that is a function of the overlap between the preferred stimulus and the cRF size. The left (right, respectively) curtain stimuli (LCs, RCs respectively) is defined as the sequence of images in which the leading edge of the curtain is moving towards left (right, respectively). A proxy of cRF centre size is estimated by detecting the images that maximize the mean firing rate (MFR) for both the LC and RC protocols.

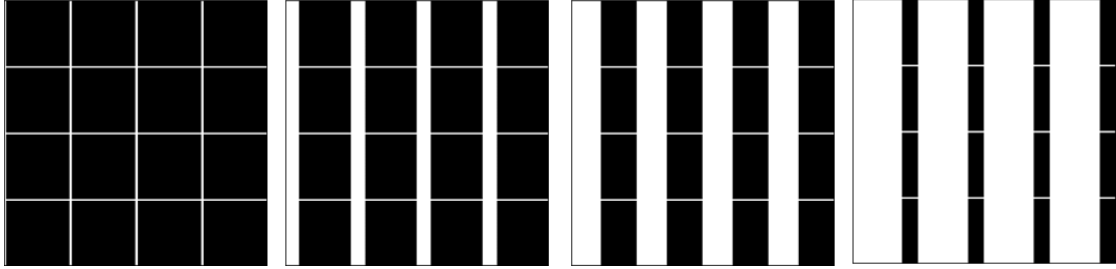


Figure 4.4: Four representative left curtain stimuli (LCs). Every 300ms the curtain steps of about $4\mu\text{m}$ enlarging from left to right.

To optimize the execution time of the protocol, the cRF estimation was parallelized by dividing the full-field stimulus in a grid of 16 areas (i.e. sub-blocks). In each block, the curtain light-stimulation protocol consists in a white curtain that spatially shifts by about $1/5$ of the electrode size ($4\mu\text{m}$) towards left for LCs, and right for RCs respectively. This gave rise to 83 images (Figure 4.4) projected for 300 ms/image, according to the physiological response of the retina, and resulting in a total stimulation time of 50s per channel. Here the closed-loop algorithm is used with the aim to speed up the characterization process: the algorithm automatically stops the projection of the curtain when the maximum peak of the MFR is found. At this point, the algorithm reverses the stimulation protocol to detect the second peak. In this way, the centre of the RF is estimated by compensating the intrinsic response delay of the RGC to the stimulus.

The algorithm performs the following operation independently for each block:

1. It quantifies the mean firing rate (MFR), i.e. the normalized number of spikes in response to each image with respect to the time-interval of the stimulus presentation. The MFR is computed for a bin size corresponding

to the 300ms duration of each stimulus. Therefore, it generates 83 different values of MFR for each electrode.

2. It smoothes the MFR obtained by applying a moving average over 5 images.
3. It computes the cRF radius as the half-difference between the positions of the white edge associated with the peaks of the firing rate occurring in the left and right curtain protocols.

So far, this method was preliminary experimentally tested only in the open loop configuration. In these experiments, the curtain spans each of the 83 positions from left to right and vice-versa.

5 Results

In this chapter I present the ground-truth validation of the detection of coincident spiking activities in simulated spike trains. I evaluated the accuracy in finding the correlation configurations between neighboring channels artificially imposed in the simulated dataset. Following the validation results, I tuned the parameters of the method for the experimental dataset and I quantified the reduction in data processing resulting from the filtering of duplicated spiking activities. Further, I evaluated the processing time required by the algorithm running on the ARM processor in the closed-loop configuration to confirm that this implemented method does not determine a significant increase of the experiment duration. Next, I classified the units identified in the data reduction step and, to validate the method, I analyzed the stability of the ON/OFF classification in subsequent iterations. Similarly to the data reduction step, I also investigated the average execution time of the algorithm and the average time required for the convergence onto a stable classification. Finally, I exploited the information acquired in the previous steps to implement a procedure to estimate in real-time the extent of receptive fields using the curtain stimulus, see Section 4.5. Here, I report preliminary results about the performances of the mapping of the receptive fields by comparing the receptive field sizes found with the state-of-the-art approach, namely Spike Triggered Average (STA). Although the code has been already implemented on the zed-board, this analysis was performed off-line, i.e. by loading the spike trains saved from previous experimental session recordings, for a fast exploratory analysis.

5.1 Data reduction

Adjacent electrodes in the HD-MEA grid are quite often recording sub-millisecond correlated spiking activities. As shown in Figure 5.1, each active electrode of the MEA shares more than 40% of spikes with at least one electrode in its 3x3 surrounding block region. Thus, the spike trains of neighbouring channels recorded with the HD-MEA exhibit sub-millisecond correlated spiking activities, suggesting that these electrodes are sensing the same source as a result of the tight spacing among nearby electrodes.

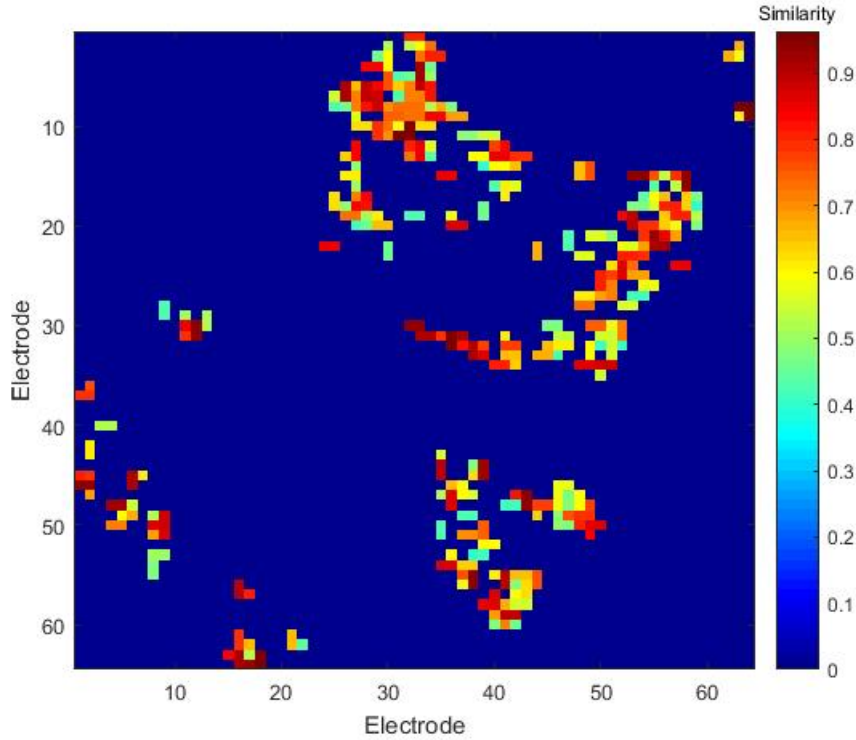


Figure 5.1: Map of the 64x64 electrodes MEA where each pixel is color coded according to the maximum similarity value in a 3x3 surrounding block of electrode. Nearly all recording electrodes exhibit highly correlated spiking activity with at least an adjacent electrode.

Consequently, a simple yet powerful strategy to reduce the complexity of the subsequent analysis is to detect such sub-millisecond correlated channels to reduce the number of electrode to be analysed. Therefore I implemented a clustering algorithm, which identifies only one leader channel for each cluster and, before applying it to real data, I tested its performances on artificially generated spike trains.

5.1.1 Validation on simulated spike trains

The analysis on simulated spike trains was carried out in order to test the cross-correlation function implemented and, importantly, to find the most suitable value of the thresholding parameter k . As expected, for increasing values of p_{add} and p_{remove} the accuracy in retrieving the correct configuration of correlated channels from the spike trains steadily increases up to its maximum value $accuracy = 1$, meaning a perfect reconstruction, obtained for $p_{add} = 1$ and $p_{remove} = 1$.

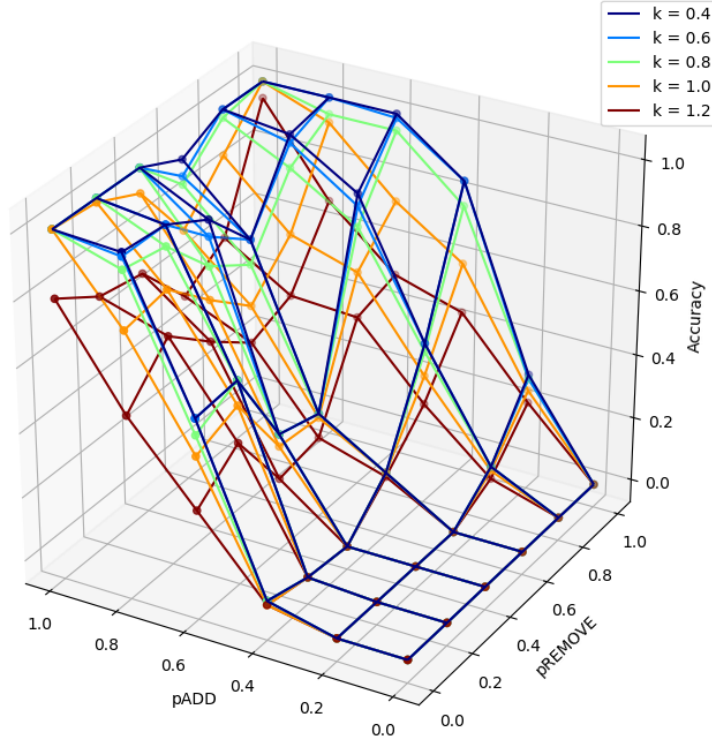


Figure 5.2: Accuracy of the algorithm in the reconstruction of the spatial correlations imposed within neighbouring channels for different values of p_{add} , p_{remove} and k in simulated dataset.

Indeed, for such values of the parameters, the two spike trains associated with the imposed configuration are exactly identical, i.e. all the spikes of a given spike train were added to the others and the non-correlated spikes were removed. In this condition, the analysis reveals that spike trains that by chance are correlated have a negligible effect on the retrieval of the correct configuration.

The clustering algorithm identifies correlated spike trains for low values of $k \leq 0.8$. A low local threshold, indeed, would also merge together those spike trains with a few spikes in common. However, even for high values of $k \geq 1.0$ the accuracy is nearly equal to 1 indicating that also with a high local threshold the algorithm groups the channels that exhibit similar spike trains.

Given these results, the value of k was set to 1 in the analysis of real data as a compromise between correctly identifying the coincident spike trains and excluding those, which although being similar, can be assigned to a more relevant cluster.

5.1.2 Performance on experimental datasets

After the validation of the cross-correlation function and the clustering algorithm, I added a closed-loop policy to stop the execution of these algorithms in order to minimize the time and the data required for the identification of the coincident spiking electrodes. To find an appropriate stopping criterion, I run the analysis in an open-loop configuration, i.e. on 300 s of spontaneous spiking activity (5 retina), to keep track of the changes after any given time-point.

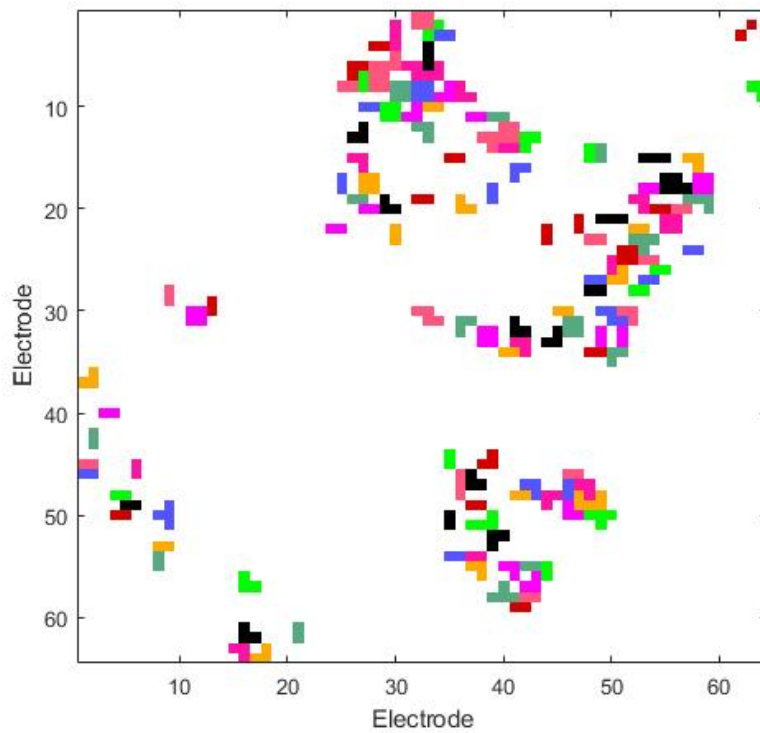


Figure 5.3: Map of clustered electrodes: adjacent electrodes that has been clustered together because exhibiting sub-millisecond correlated spiking activity are represented with the same color.

An illustrative example of the clusters detected by considering the entire experiment (300 s of spontaneous activity) is shown in Figure 5.3. In this representation, adjacent channels that exhibit coincident spiking activities are depicted in

the same colour. Hence, the dimensionality of large-scale recordings can be reduced by clustering adjacent active electrodes that exhibit correlated spike trains and by considering for further analysis only the leader electrodes, i.e. the ones with the highest spiking activity of each identified clusters.

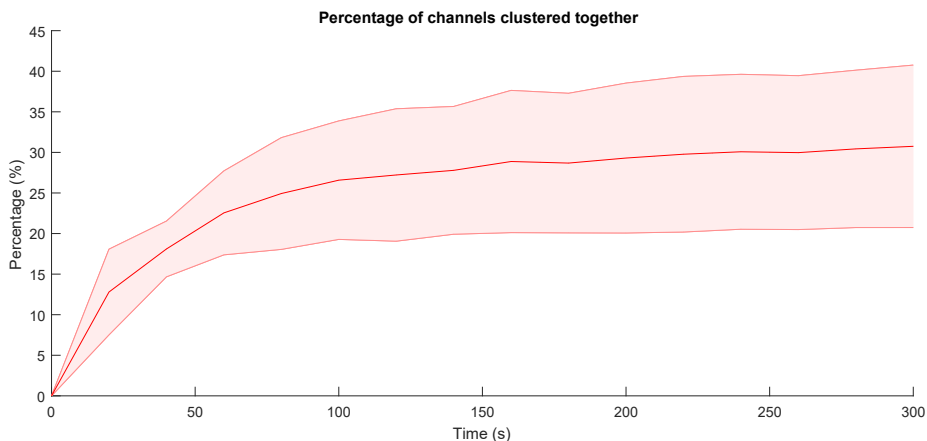


Figure 5.4: Mean percentage of electrodes clustered together with respect to the total number of active electrodes. The shaded area represents the standard error.

To test the stability of the algorithm and to find the experimental recording time required to achieve a stable configuration of clustered channels I quantified the number of leader electrodes detected at each iteration (Figure 5.4) and the number of differences between two consecutive iterations of the clustering algorithm. In this way, I could evaluate whether providing more information to the clustering algorithm, i.e. by adding a 20 s time-interval of recorded spiking activity, would significantly change or not the previous cluster arrangement. Within the first 20 seconds of recording the number of leader electrodes decrease significantly, indicating that the algorithm detects several groups of electrodes exhibiting similar spiking activity. After 120 s, the leader electrode arrangement reaches a stable configuration determining an average reduction of the active electrodes of $\sim 30\%$ respect to the initial number of AEs.

The closed-loop policy results in an average stopping time of 120 s. Afterwards, the arrangement of the clusters remained substantially stable, with an average mismatch along the subsequent time intervals of $1.5 \pm 0.4\%$ (Figure 5.5, green).

Importantly, by occupying the CPU for 22.9 ± 1.5 ms per second of neuronal recording, this algorithm provides a quick identification of redundant information, reducing the large amount of data acquired for the following analysis.

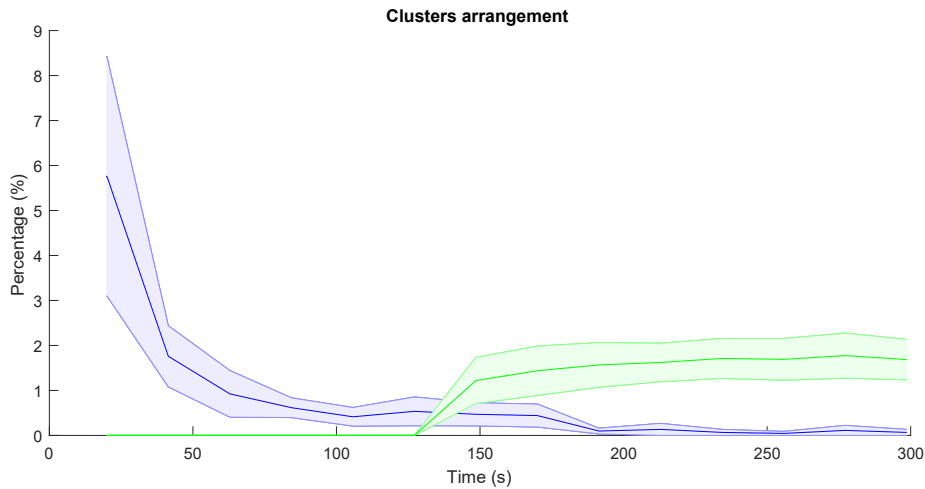


Figure 5.5: Percentage of clustering variation after each 20 s of recording (blue). Percentual variation of the clusters after the stopping criterion is met (green).

5.2 RGCs classification

After the identification of the leader electrodes in the previous algorithm, they were classified in ON or OFF RGCs according to their preferential response to white or black full-field flashes.

The mean firing rate (MFR) of two representatives RGCs in response to black and white flashes is depicted in Figure 5.6: ON RGCs sharply increases their MFR during increase in light intensity, as during the white flash, and vice-versa the OFF RGCs increase their MFR as a consequence of a decrease in light intensity, e.g. a black flash.

To classify each leader electrode according to these two behaviours, the closed-loop algorithm implemented here, first stimulate the retina with a white and black flashes and based on the spike count balance between the white and black phase assign each LE to the appropriate sub-type, see Section 4.4. To increase the accuracy of classification, the algorithm continuously iterate these two steps and requires a stopping criteria.

To stop the execution of the classification algorithm I quantified the changes in the classification between consecutive iteration of visual stimulation. The number of LEs switching from ON to OFF and vice versa in consecutive iterations steadily decrease after a few cycles of stimulations, see Figure 5.7, and converges after only 7.25 ± 3 steps. Moreover, further stimulation following the convergence point, would not significantly change the ON-OFF classification as the number of mismatches remains bounded by the convergence-threshold.

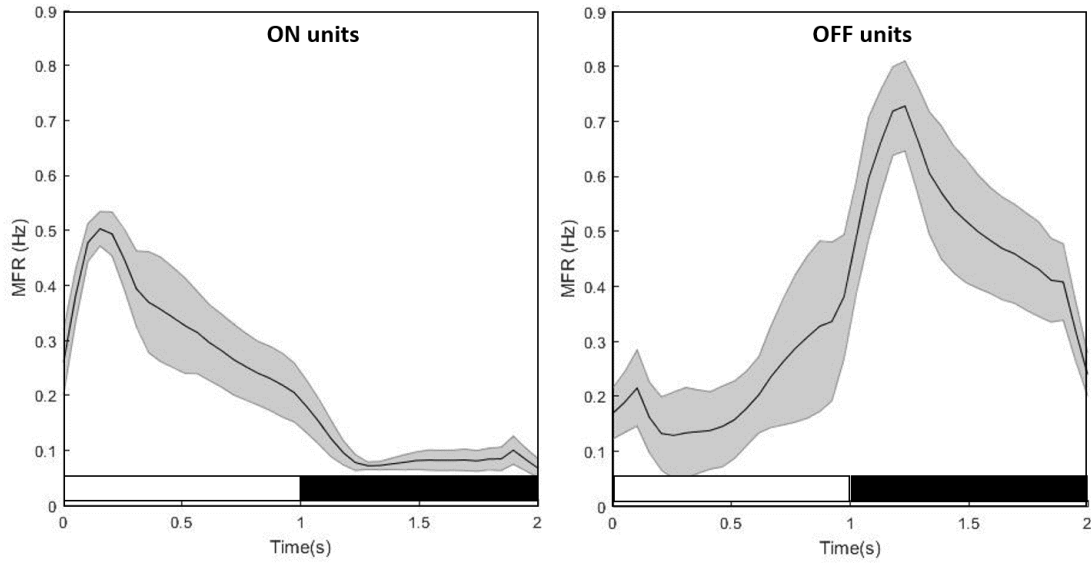


Figure 5.6: Representative response of an ON and OFF RGC to black and white flashes as detected by the implemented algorithm. Below the cells responses is reported the corresponding projected flash stimulus.

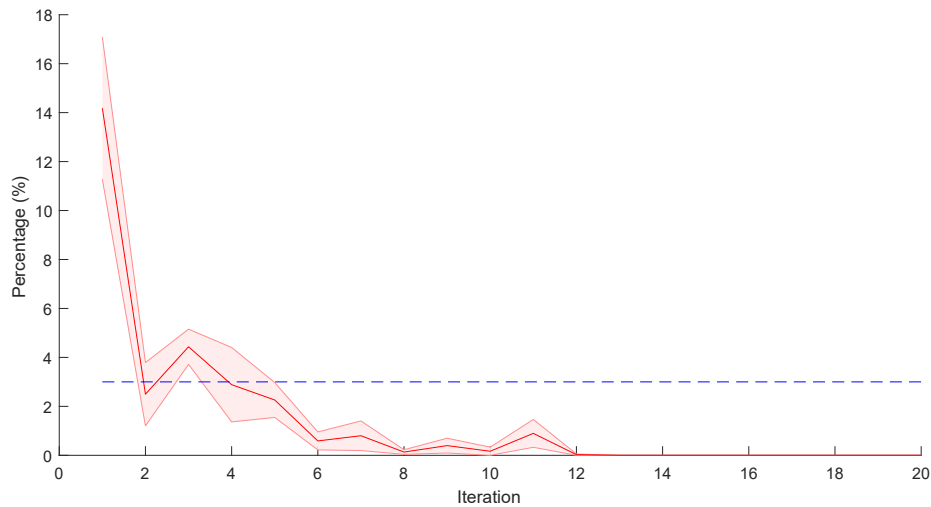


Figure 5.7: Mean percentage of switching electrodes with respect to the total active electrodes for each stimulation phase. The shades area represents the standard error.

In this way, by taking advantage of the closed-loop hardware, the algorithm tailor the number of stimulation cycle in order to acquire enough information for

classifying the leader electrode identified preventing from wasting of experimental time.

5.3 Estimation of RF RGCs

Finally after the identification and the classification of the leader electrodes, I implemented a heuristic strategy to estimate their receptive field size by exploiting the spatio-temporal response dynamic of RGCs to a curtain stimulus described in Section 4.5.

As shown in Figure 5.11, the response of an illustrative ON RGC to a sliding curtain stimulus is characterized by a single peak for each direction of movement. Thus, the RF can be adequately estimated by considering the half-difference between the positions of the white edge (x-axis) associated with the two peaks.

To test the goodness of this method, I compared the cRFs estimation with the one obtained using the Spike Triggered Average (STA), for both ON and OFF RGCs, see Figure 5.9 and Figure 5.10. In this representation, an ideal cRF estimation would result in the alignment of points along the diagonal (dashed red line in Figure 5.9A and Figure 5.10A). However, a linear regression (orange line) shows that the current implementation of this approach has several limitations and requires further optimizations. This is further confirmed by the error quantification between the STA and our estimation, as shown in Figure 5.8.

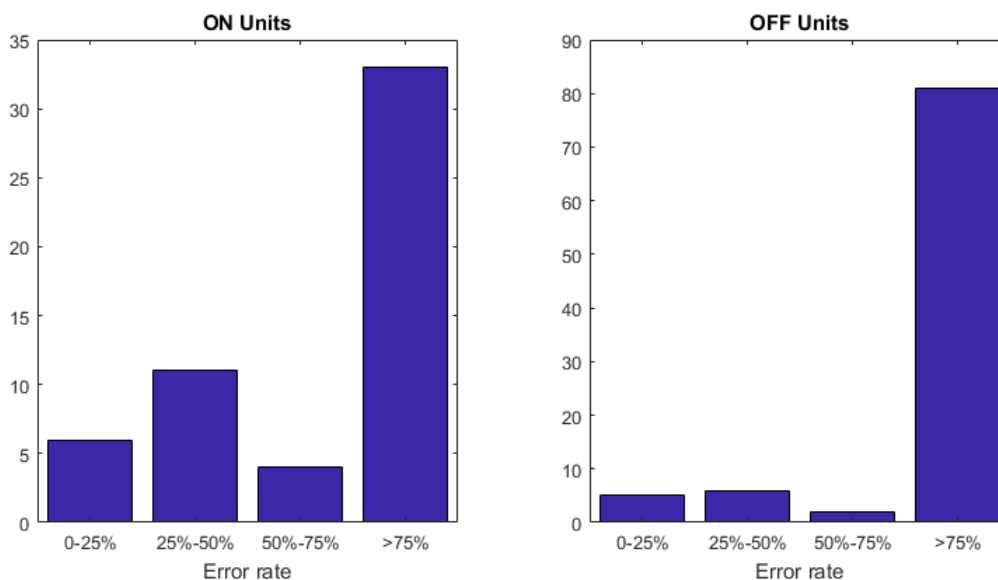


Figure 5.8: Distribution of the RF radius estimation error between STA and the curtain protocols for ON and OFF RGCs.

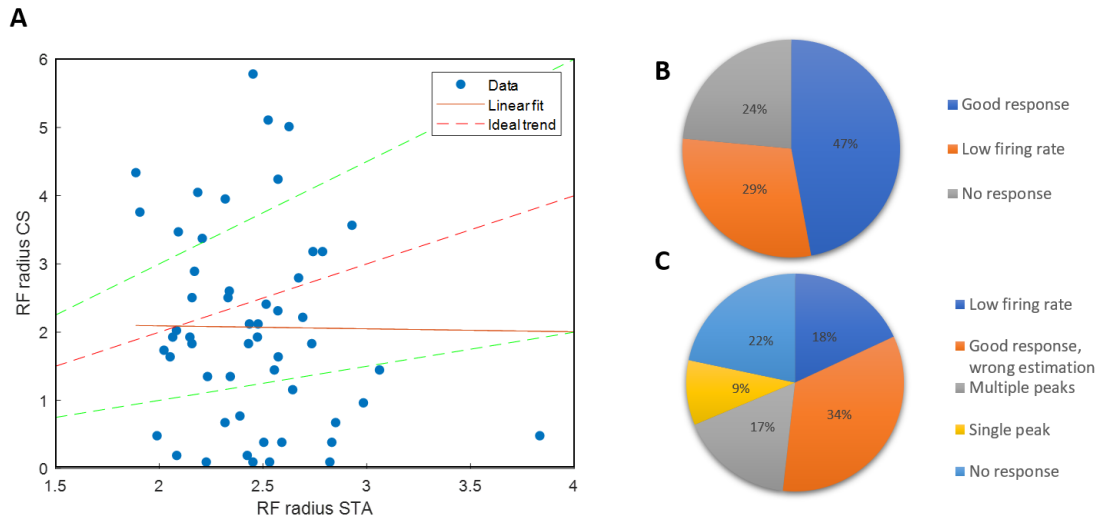


Figure 5.9: Comparison between the radius of the receptive field estimated with STA and with the curtain stimulus for the ON units population. (A) Representation of the distribution of the radius estimation between the two approaches. (B) Pie chart of the radius of the RF estimated with an error with respect to the ground-truth lower than 50% (data distributed between the two green dashed lines in (A)). (C) Pie chart of the population outside the region delimited by the two green dashed lines in (A).

Considering only the RGC whose estimation differed from less than 50% from ground-truth data (green dashed lines in Figure 5.9A and Figure 5.10A, for ON and OFF cells respectively), I visually inspected their response behaviour to the curtain stimulus to investigate whether, in such a restricted case, the physiological principle underlying the estimation algorithm used holds true. To disentangle different behaviours I classified the RGCs in three major classes (Figure 5.9B and Figure 5.10B):

good response cells characterized by a spiking response in line with what we expect (blue);

low firing rate cells exhibiting a small number of spikes, i.e. lower than 30 spikes during the whole recording (orange);

no response cells that even showing a well defined spiking activity are not recapitulating the features of the expected response for this type of stimuli (grey).

For both the ON and OFF populations the most of RGC responses (47% ON, 55% OFF) were characterized by the two peaks, providing a proof of concept that

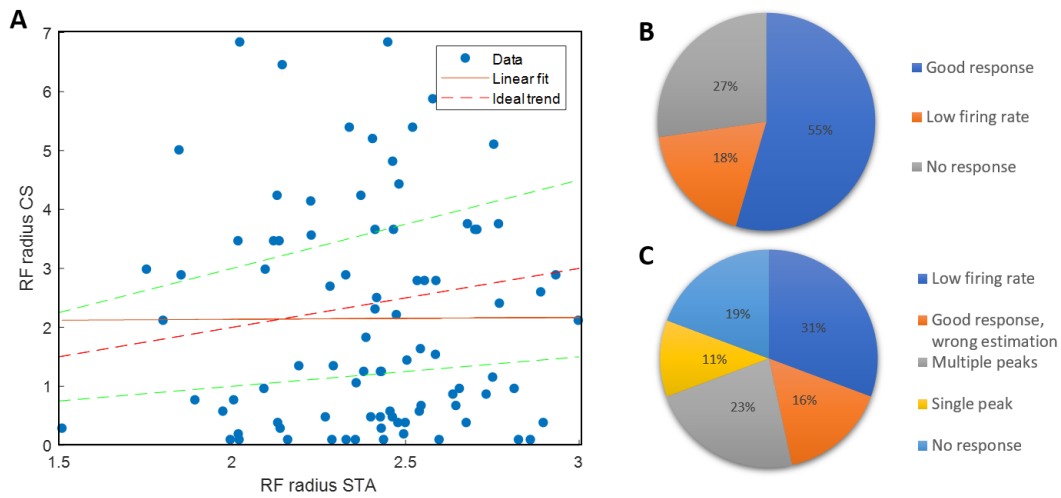


Figure 5.10: Comparison between the radius of the receptive field estimated with STA and with the curtain stimulus for the OFF units population. (A) Representation of the distribution of the radius estimation between the two approaches. (B) Pie chart of the radius of the RF estimated with an error with respect to the ground-truth lower than 50% (data distributed between the two green dashed lines in (A)). (C) Pie chart of the population outside the region delimited by the two green dashed lines in (A).

the proposed algorithm is a promising strategy for receptive field estimation. However the remaining 53% ON and 45% OFF represent two cases of false positive estimation. In the 29% ON and 18% OFF the radius of the RF was well estimated even though the firing rate of the cells was not enough for a correct characterization of the cells activity. These cells show a weak spiking activity during all the recoding with some peaks of 5/6 spikes, thus the algorithm computes the RF radius considering these peaks although they are not characterizing the RF center. Instead in the 24% ON and 27% OFF the cells do not exhibit a modulation of their activity according to the visual stimulus but the radius was correctly estimated. They exhibit a high and continuous spiking activity and for the computation of the RF center size the algorithm considers the first peak founded in each direction of the stimulus achieving a right, but theoretically incorrect, RF estimation.

Representative examples of the three cells behaviours described are reported in Figure 5.11.

On the other hand, regarding the RGCs that significantly differed from the ground-truth estimation (outside the green dashed lines) I found, upon visual inspection, five distinguishable principal behaviours, see Figure 5.9C and Figure 5.10C:

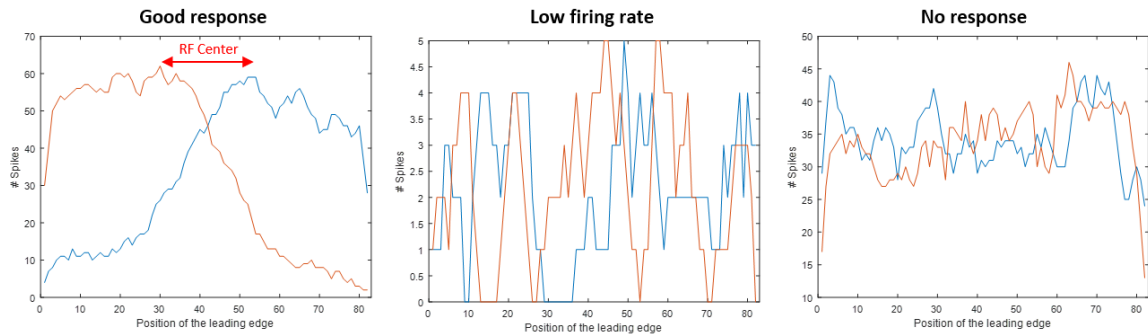


Figure 5.11: Representative response of three retinal ganglion cells to the sliding curtain stimulus identified for the classification in the three classes *Good response*, *Low firing rate* and *No response*.

low firing rate with a poor spiking activity, i.e. lower than 30 spikes during all the recording (blue);

good response, wrong estimation that responded adequately and in-line with their expected physiology to the stimulus but the method used for the estimation of the size of the RF is not adequate (orange);

multiple peak with multiple peaks in their response (grey);

single peak with a single peak of response, i.e. the firing rate peak was found in only direction of the curtain stimulus (yellow);

no response which include the RGCs whose response was not clearly satisfying any of the mentioned criteria (light blue).

Representative examples of the three cells behaviours described are reported in Figure 5.12. In this cases the 18% ON and 31% OFF the low firing rate of the cells leads to the wrong estimation of the RF radius. Here the limit regards the curtain stimulus implemented that is not able to evoke a strong firing of the cells thus the algorithm for the calculation of the RF radius fails.

An interesting case is represented by the 34% ON and 16% OFF in which the estimation of the RF size fails due to the algorithm implemented: the cells present a behaviour in accordance to the model of their response to a curtain stimulus, but the RF radius estimated as the half-difference between the position of the leading-edge of the two peaks is incorrect. The visual investigation that I have performed lead to the conclusion that most of the cells included in this class are those that are on the right or left edge of the HD-MEA, indeed as can be seen in Figure 5.12,

they are characterized by two peaks at the very beginning of the projection of the stimulus. Here the radius is estimated as big as the entire HD-MEA.

Another important case is the third class where are included the cells (17% ON and 23% OFF) which present a behaviour characterized by multiple peaks. These multiple peaks could represent the maximum response of different cells, since the same channel can sense different, very close units.

The 9% ON and 11% OFF of the all population is represented by the cells which response present a single peak in one of the two directions of the curtain stimulus. In this class are probably included also some units located on the border of the HD-MEA thus in one direction of the stimulus they present the characteristic peak of the theoretical model but during the inversion of the stimulus they are not responding as expected.

Finally, in the last class were included all the cells (22% ON and 19% OFF) whose behaviour is characterized by a constant tonic firing rate, thus the algorithm was not able to identify the peaks for a correct estimation of the RF size.

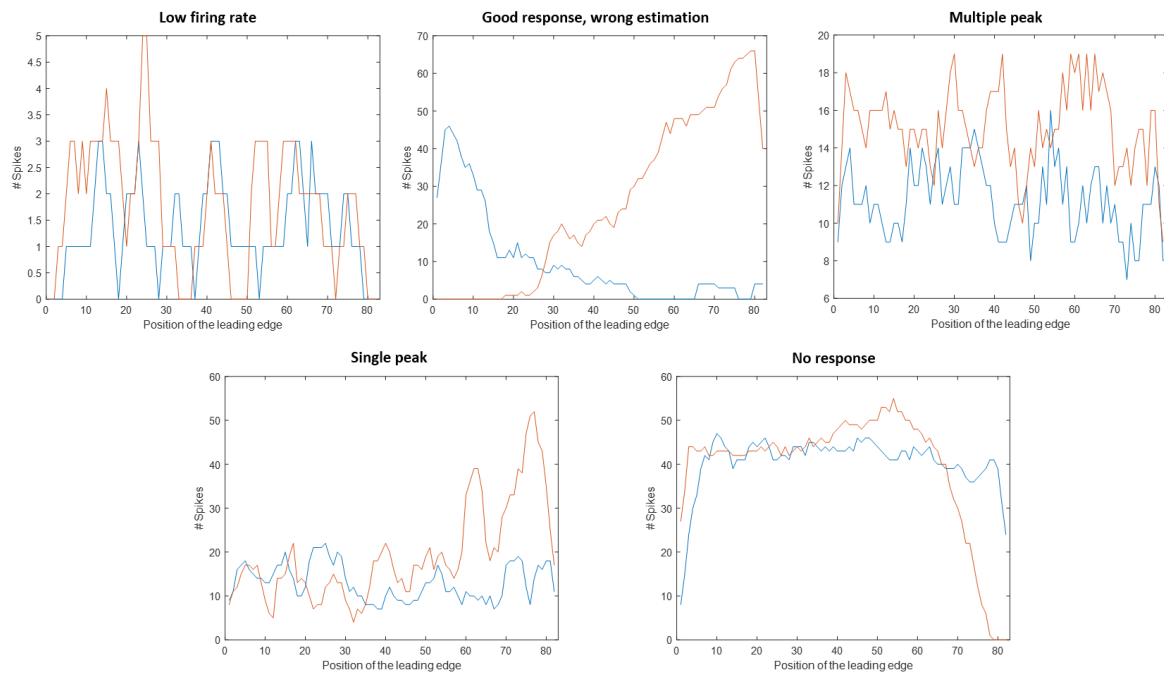


Figure 5.12: Representative response of five retinal ganglion cells to the sliding curtain stimulus identified for the classification in the five classes *Low firing rate*, *Good response, wrong estimation*, *Multiple peak*, *Single peak* and *No response*.

As quantified above, the accuracy of the current approach is still inadequate for the experimental needs and this algorithms needs further optimizations. Some

intrinsic characteristics of the units, as a continuous and high firing rate or oppositely the low number of spikes elicited by the stimulus, lead to a incorrect estimation of the RF. Instead when the cells exhibit a high firing rate and the expected response characterized by the two peaks, one for each direction of the stimulus, even for a very low number of cells, the algorithm presented here was able to correctly estimate the size of the receptive field center. Thus, this approach is promising, but it requires following studies considering, for instance, different strategies of visual stimulation compared to the simple one explored in this work. Possible directions to explore in future work are discussed in Section 6.1.

6 Conclusion

Visual perception is the ability to interpret the surrounding environment using the light in the visible spectrum reflected by the objects. The first stage of this process takes place in the retina, where photoreceptors encode and convey visual information to retinal interneurons and finally to retinal ganglion cells (RGCs), i.e., the output neurons of the retina, for further processing. As a consequence of this pre-processing, the RGCs are tuned to particular visual features, such as motion in a particular direction, oriented lines, or colour contrast and transmit to the brain only features of the visual scene, rather than a discretized pixel-like image as a standard camera does. Indeed, how the retina, and in particular the different types of RGCs, encodes the information of the visual images is still unclear.

Therefore, in this Master's Thesis, I worked on developing original analytical tools that can be implemented in real-time hardware to investigate, describe and characterize some of these functional properties expressed by retinal ganglion cells. As the overall nervous system, feedbacks and closed-loop controls from retinal neurons modulate the RGCs spiking activity. Consequently, an appropriate method to approach and understand the retinal output is to implement closed-loop experiments, i.e., to provide visual stimuli based on the instantaneous spiking activity of the retinal ganglion cells. To do so, I carried on my studies at the Italian Institute of Technology (IIT) to exploit a closed-loop platform in combination with high-density recordings developed in the NetS3 Lab. This platform exploits the FPGA/CPU resources of a Xilinx ZedBoard Zynq-7000 and perform pre-processing tasks, such as signal conditioning, filtering and spike detection, with a maximum latency of 2 ms. Thanks to this platform it is possible to handle the large stream of data generated by the new generations of high-density microelectrodes arrays (HD-MEA) based on CMOS (Complementary Metal-Oxide-Semiconductor) technology, which integrate active on-chip read-out circuits to record the extracellular potential of several thousands of closely spaced microelectrodes.

To provide dedicated tools for investigating retinal function, I had to face a computational challenge to fulfil the closed-loop time and memory constraints that lead me to optimize how the data are acquired. Indeed, the tight spacing among

adjacent electrodes of HD-MEAs result in the duplicate detection of the same retinal ganglion cell in multiple neighbouring electrodes. Therefore, to reduce the computational load of subsequent analysis, I implemented an on-board pseudo-real-time algorithm that provide an effective downsampling of the array to remove those electrodes that are exhibiting coincident spiking activities. To this aim, I optimized a cross-correlation function to detect pairs of electrode sharing spikes at sub-millisecond resolution in pseudo-real time (about 22.9 ± 1.5 ms per second of neural recording) and I devised a simple, yet powerful, clustering procedure to group multiple correlated electrodes.

To validate the implemented algorithm, I proved, through simulations of the RGCs spiking activity, that if I impose a certain spatial configuration of correlated channels on a random set electrodes, the clustering algorithm is able to detect and reconstruct its spatial organization. Thanks to the results obtained *in silico*, I found an optimal set of parameters and, with these settings, I applied the algorithm on HD-MEA recordings of retinal ganglion cells spiking activity of *ex vivo* mouse retina. By identifying and removing duplicate spikes recorded by adjacent electrodes of HD-MEA, I found that the filtering procedure significantly reduced by $\sim 30\%$ the computational cost required for closed-loop investigations. Given the closed-loop capability of the platform, I also implemented a closed-loop policy to stop the execution of this algorithm when the data acquired are enough to achieve a stable downsampling of the electrode matrix. With this policy, the algorithm stops within 120 s and provide a substantially stable downsampling configuration of the electrode matrix with an average mismatch in the subsequent time intervals of $1.5 \pm 0.4\%$.

Next, I have implemented a second closed-loop algorithm that controls visual stimuli to infer major functional types of retinal ganglion cells. In detail, based on the spiking response to white and black stimuli, the algorithm classifies the leader electrodes (identified with the first algorithm) in ON- or OFF-type retinal ganglion cell's responses. A closed-loop policy ensures that enough information is acquired by iterating the white/black cycle of visual stimulation. Even if the computational time dedicate to this task is reasonably short (117.3 ± 30.9 ms to analyse the results for each iteration), the overall time spent on this task, ≤ 10 s, is mainly ascribable to the retinal physiology. Indeed, I found that the algorithm requires 7.25 ± 3 iterations of visual stimulations to characterize the preferential response of RGCs.

In the third part of my study, I evaluated a potential approach for estimating the retinal ganglion cells receptive field size in real-time and in closed-loop. State-of-the-art approaches are highly time-consuming for an accurate and precise estimation of the receptive fields. Indeed, they require a rather long visual stimulation, consisting of a large number of stimuli, that prevent from performing many

other experimental phases because of a limited retinal viability after dissection. In addition, since neurons process information on a few millisecond time-scale, one could be interested in tracking receptive field size changes over time.

Therefore, the approach that I have developed, based on receptive field physiological properties, aims at minimizing the experimental time and the amount of data required for the receptive fields characterization. In a preliminary exploration, we have found that even though the approach was promising, it resulted in acceptable estimations only for a $\sim 15\%$ of retinal ganglion cells, which response was characterized by a high firing rate and the two peaks expected. I diagnosed that the poor performances are mainly imputable to the stimulation protocol that was not able to evoke sufficiently reliable responses in RGCs, i.e. the cells present a low firing rate to the stimulus or exhibit a high and continuous spiking activity. In these cases the approach used for the estimation of the radius of receptive field as the half-difference between the position of the leading-edge of the two peaks leads to an incorrect value due to the intrinsic activity of the cells. Therefore, this current implementation fails for the cells on the borders of the HD-MEA indeed in this case the radius is estimated as almost all the dimension of the HD-MEA. Thus the described algorithms can be improved for a more extended classification of RGCs and for a better estimation of their receptive fields. Possible directions for future studies aimed at improving the performances of this closed-loop algorithm are discussed in the next section.

6.1 Discussion

In this work the large amount of data acquired with HD-MEAs has been treated as an issue proposing an algorithm for the data reduction. This because in real-time applications these redundant information leads to waste of computational resources in analyzing duplicate spike trains. Thus, given the low time required for the processing time of the algorithm is suitable for real-time applications. A further improvement is to clean the discarded channels from coincident spikes to unveil the probable spiking activity of new units. However, in a real-time application this approach can lead to some waste of time because, is necessary to assess for each spike its membership to a spiking unit. Coincident spikes detected in the discarded channels can also be exploited for estimating the position of the retinal ganglion cell and consequently to implement a position based spike sorter, possibly in real-time.

The first implementation of the algorithm for the classification of the RGCs is very basic and easy. It is estimated that there are over 30 different RGC types in the mammalian retina [60] each one represent a specific information about the visual scene and encode it through spike trains. For example, just the ON-type

cells can be classified in more than 10 subtypes according to their response kinetics, their selectivity in the direction or orientation of a moving objects [60].

The classification of the RGCs can be refined using different stimuli, such as bars moving in cardinal directions, the preferential response of the RGCs to other features, such as direction selectivity, can be probed.

The current implementation of the closed-loop algorithm for the receptive fields estimation prevent from correctly identifying the RF size in a large number of RGCs. This can be due to the low rate of evoked spikes or to issues due to multiple response peeks. Possible solutions can take into consideration the use of different stimuli or different analysis for the mapping of the RF. Given the high number of cells that exhibit the low number of spikes elicited by this kind of stimulus, first it could be applied several times and average the responses of each cell in order to verify the model of response explained in Section 2.3.

If the curtain stimulus continues to be unsuitable for the purpose, it can be substituted with full-field moving bars of different spatial frequencies cycling at 1 Hz in different directions. Previous work showed that with this type of stimuli we can estimate with fairly good accuracy the RF centre size. In this framework, a closed-loop policy would result in a reduction of the stimuli required for the cRF estimation convergence, avoiding unnecessary iterations of the protocol. The time saved could be used to rotate the bar motion direction to provide a more accurate estimate of the RFs ellipsoidal shape. Moreover, with this approach, the RF of nearly all channels can be quantified simultaneously thanks to the few computations and small memory storage required.

Further development for RF estimation algorithms can include a total parallelization for all the RGCs identified in order to reduce more and more the execution time of the algorithm.

Finally, it has to be noted that together with recently developed implantable CMOS-probes for in-vivo high-resolution recordings [61], similar approaches might be applied in the future works to other brain circuits to infer their structure-function organization or to develop bioelectric therapeutic devices.

Annex I Experimental setup

This Section contains detailed information on the hardware that I used as a starting point for this work. Additionally, I report the experimental procedure used by my colleagues of the NetS³ laboratory (Fondazione Istituto Italiano di Tecnologia) to gather the spiking activity from ex-vivo retina for a self-consistent thesis.

Acquisition unit

RGCs bioelectrical activity was acquired using ARENA BioChips (3Brain AG, Wädenswil, Switzerland), which are HD-MEAs based on the Active Pixel Sensor concept, see Figure 1B. This platform can simultaneously record from 4096 square electrodes of $21 \times 21 \mu\text{m}^2$ size arranged in a 64×64 grid of $42 \mu\text{m}$ pitch, resulting in a total active area of $2.67 \times 2.67 \text{mm}^2$. From each of the 4096 electrodes, this device samples the extracellular potential at a frame rate of 7.022 kHz.

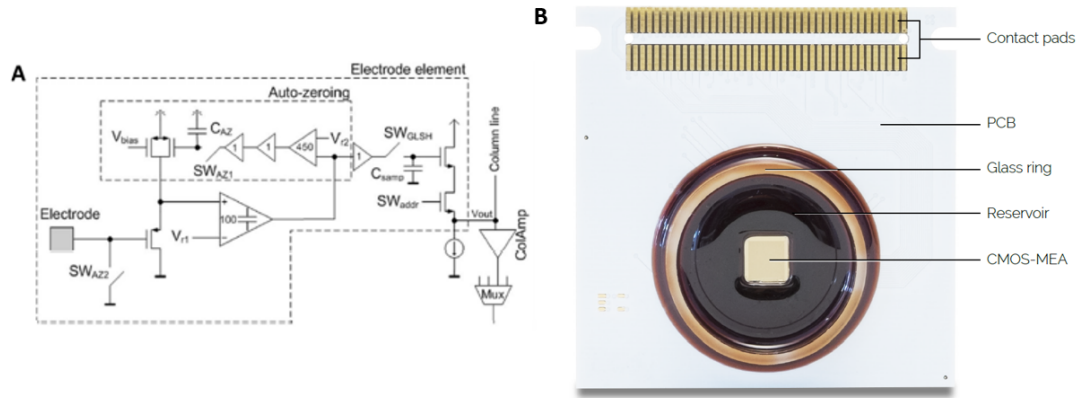


Figure Annex I.1: APS-MEA CMOS chip. (A) Representation of the signal amplification chain and of the electrode readout. (B) BioChip from 3Brain.

The metal electrodes are made of aluminum-alloy and post-processed with

noble metals, e.g. gold or platinum, to increase the electrode sensitivity. The active circuitry of the electrodes is insulated from the extracellular environment with a silicon oxide and silicon nitride layer, which fully coat the sensing area of the device except for the electrode areas. Since the BioChip is based on the APS concept, the signal is locally adapted from high impedance (electrode-side) to low impedance (wiring-side) to avoid the induction of coupling noise from electrical wiring before amplification thanks to in-pixel amplifiers, 40dB gain, placed underneath each electrode (Figure 1A). On-chip multiplexing and addressing circuits prevent from individually wiring each electrode off-chip. Indeed, even though the number of simultaneously recorded electrodes easily exceed a few thousands of elements, with this strategy the number of wiring outputs remains bound to a few tenths of outgoing connections.

CMOS devices are also photosensitive, photo-generated charges can give rise to different DC drifting that can saturate in-pixel amplifiers. To overcome this issue, the BioChips in-pixel circuit integrates a calibration process that consists of an auto-zeroing circuit. This system allows a dynamic calibration of the electrode DC voltage to prevent amplifiers from saturation. To do so, the calibrated DC voltage is subtracted from the electrode signal before the first amplification stage. This process allows adapting the circuit performance to different experimental conditions. In particular, under light stimulation conditions, as this work requires, the light-induced amplifier saturation can be further mitigated by using higher calibration frequencies to keep the DC input signal as close as possible to the working point of the amplifier.

A reservoir chamber, limited by a glass ring, enclose the active sensing area of the chip in order to maintain viable neuronal tissue as neuronal cultures or ex-vivo brain circuits either under cell culture media or perfused media during the experiment.

The contact pads of the BioChip allow a stable connection between the BioChip and the BioCAM X. The latter is a platform allowing the acquisition from all the 4096 recording sites of the CMOS-MEA planar device with sub-millisecond resolution. The BioCAM X performs analog to digital conversion of the signal, with a resolution of 12 bit, which is continuously sent to the real-time processing unit and to an offline processing unit through through a Camera Link connection.

On the offline processing unit the acquired data are visualized with the software BrainWave X (from 3Brain, AG). In Figure 2 shows a screenshot of the software during a typical experiment: the MEA Viewer is in a one to one connection with the electrodes in the MEA grid and each of its pixels is color-coded according to variations in the extracellular potentials recorded by the electrode located in the same position of the MEA grid.

The data are stored in HDF5 hierarchical data format and are easily accessible

from the numerical computing environment MATLAB for offline data analysis.

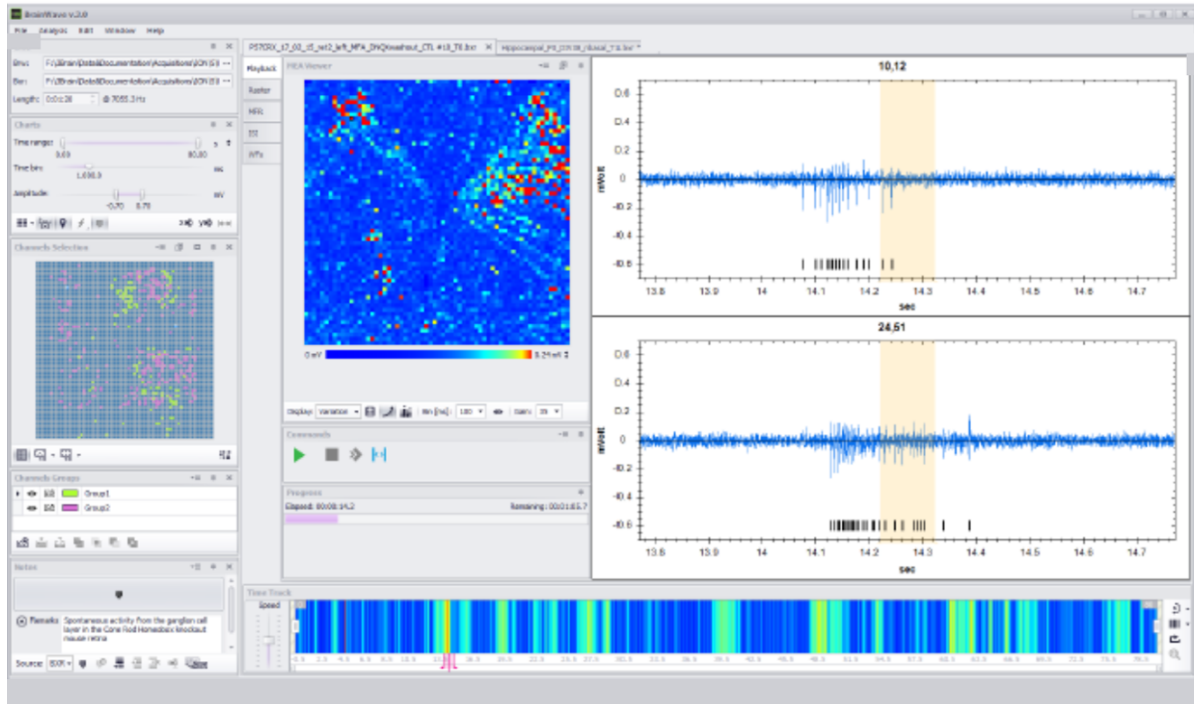


Figure Annex I.2: BrainWave software visualization.

Processing unit

The main characteristic of this system is the ability to exploit parallel processing in order to achieve high performance and low latency. The Xilinx Zynq is based on the integration of the software programmability of an ARM-based processor with the hardware reconfigurability of a Field Programmable Gate Array (FPGA). This unit consists of three major components shown in Figure 3:

- programmable logic and hard-wired blocks;
- Zynq processing system;
- DDR memory.

The first component is programmed to de-serialize the data received from the acquisition unit through the Camera Link interface and subsequently the raw data are filtered and processed in order to detect the neural spikes.

The filtering process is implemented by a band-pass FIR filters with cut-off frequencies placed at 300 Hz and 3400 Hz. The system integrates 32 FIR blocks to

permit the filtering of 4096 input channels, divided into groups of 128 channels for each block in order to minimize the resources usage.

The spike detection step is based on an amplitude threshold that is estimated according to the standard deviation of the filtered signal for each extracellular trace. To take into account modulations of noise amplitudes independently occurring in multiple signals, the threshold is dynamically adapted to the current noise level of the signal. Finally, the filtered signal and the detected spike are stored in the DDR memory.

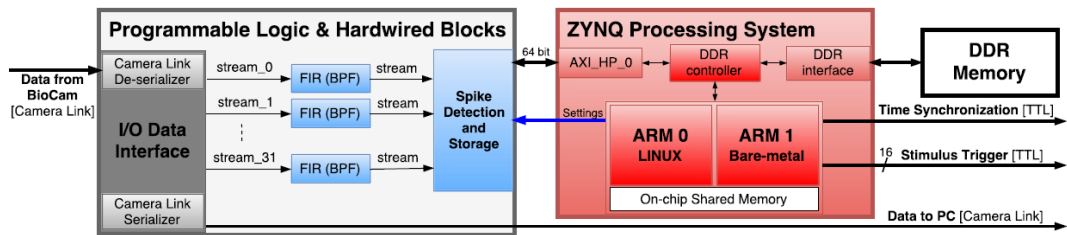


Figure Annex I.3: Schematic block diagram of the Zynq-based Real-time Processing unit consisting of three major parts: Programmable Logic and Hardwired Blocks, a Zynq Processing System and, a DDR Memory.

The Zynq processing system integrates the dual-core ARM Cortex-A9 processor sharing a 512 MB DDR memory. The first core is dedicated to a Linux-based operating system that provides a user interface and network connectivity for system initialization, a programmable logic for clock configuration and management, and a toolbox for setting the bare-metal core management/communication tasks.

The second core has real-time access to the DDR memory where the timestamps of the detected spikes are stored. This bare-metal core is used to run the decisional as well as closed-loop algorithms, described with general programming languages as C.

Optical stimulation

Concerning the optical stimulation to evoke visual responses in the retina, additional hardware blocks for streaming a video output to a High-Definition Multimedia Interface (HDMI) has been implemented on the programmable logic. These blocks periodically read from a dedicated section of the DDR memory, and, with a refresh rate of 60 Hz, stream one image consisting of 684x608 pixels with 24-bit RGB depth, through the HDMI port to a Digital Light Projector (LightCrafter, Texas Instruments Inc., USA). To change the image and thus the stimulus, the

ARM processor updates the DDR memory section with new values according to the visual stimulation algorithm.

Ex-vivo retina preparation

Ethical statement All the experiments on ex-vivo retina were performed in accordance with the guidelines established by the European Community Council (Directive 2010/63/EU of 22 September 2010). All procedures involving experimental animals were approved by the institutional IIT Ethic Committee and by the Italian Ministry of Health and Animal Care (Authorization number 110/2014-PR, December 19, 2014).

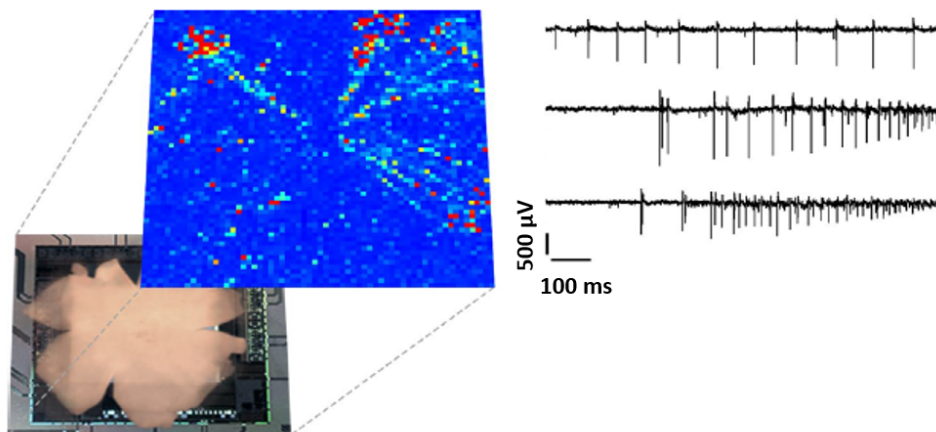


Figure Annex I.4: Mouse retina displaced on the HD-MEA. Retinal ganglion cell activity is colour coded.

Retina dissection Five six weeks old C57BL/6 male mice were dark-adapted for twelve hours and subsequently anesthetized with CO₂ and sacrificed by cervical dislocation. Similarly as in [4], upon eyeballs enucleation, cornea, crystalline, sclera and vitreous were accurately removed to isolate the retinal tissue. Next, the retina was placed onto a CMOS-MEA with the retinal ganglion cell (RGC) layer in contact with the electrodes, leaving the photoreceptor layer exposed. Prior to the retinal placement, devices were pre-conditioned by filling their reservoir with Neurobasal for two hours at 37°. A polyester filter (Sterlitech Corp., Kent, WA, USA) and a circular anchor were then placed onto the photoreceptor layer to hold in place the retina. To ensure retinal vitality throughout the experiments, a constant

flow of media (AMES media - Sigma - Merck KGaA, Darmstadt, Germany) supplemented with 1.9g/L of sodium bicarbonate equilibrated with carboxigen (95% O₂ and 5% CO₂) was perfused into the well by using a peristaltic pump (~1 ml /min).

Bibliography

- [1] Gollisch T, Meister M (2010) Eye Smarter than Scientists Believed: Neural Computations in Circuits of the Retina. *Neuron* 65: 150–164.
- [2] Masland RH (2001) The fundamental plan of the retina. *Nature Neuroscience* 4: 877–886.
- [3] Fiscella M, Farrow K, Jones IL, Jäckel D, Müller J, et al. (2012) Recording from defined populations of retinal ganglion cells using a high-density CMOS-integrated microelectrode array with real-time switchable electrode selection. *Journal of Neuroscience Methods* 211: 103–113.
- [4] Hilgen G, Pirmoradian S, Pamplona D, Kornprobst P, Cessac B, et al. (2017) Pan-retinal characterisation of Light Responses from Ganglion Cells in the Developing Mouse Retina. *Scientific Reports* 7: 1–14.
- [5] Berdondini L, Imfeld K, Maccione A, Tedesco M, Neukom S, et al. (2009) Active pixel sensor array for high spatio-temporal resolution electrophysiological recordings from single cell to large scale neuronal networks. *Lab Chip* 9: 2644-2651.
- [6] Shapley R (1982) The Contrast Gain Control and Feedback Within the Retina. *IFAC Proceedings Volumes* 15: 489–494.
- [7] Tranchina D, Gordon J, Shapley RM (1984) Retinal light adaptation - evidence for a feedback mechanism. *Nature* 310: 314–316.
- [8] Miranda-Domínguez O, Gonia J, Netoff TI (2010) Firing rate control of a neuron using a linear proportional-integral controller. *Journal of Neural Engineering* 7: 066004.
- [9] Müller J, Bakkum DJ, Hierlemann A (2013) Sub-millisecond closed-loop feedback stimulation between arbitrary sets of individual neurons. *Frontiers in Neural Circuits* 6: 121.

- [10] Wallach A (2013) The response clamp: functional characterization of neural systems using closed-loop control. *Frontiers in neural circuits* 7: 5.
- [11] Wagenaar DA, Madhavan R, Pine J, Potter SM (2005) Controlling bursting in cortical cultures with closed-loop multi-electrode stimulation. *The Journal of neuroscience : the official journal of the Society for Neuroscience* 25: 680–8.
- [12] Bölinger D, Gollisch T (2012) Closed-Loop Measurements of Iso-Response Stimuli Reveal Dynamic Nonlinear Stimulus Integration in the Retina. *Neuron* 73: 333–346.
- [13] Seu GP, Angotzi GN, Boi F, Raffo L, Berdondini L, et al. (2018) Exploiting All Programmable SoCs in Neural Signal Analysis: A Closed-Loop Control for Large-Scale CMOS Multielectrode Arrays. *IEEE Transactions on Biomedical Circuits and Systems* 12: 839–850.
- [14] Chichilnisky EJ (2001) A simple white noise analysis of neuronal light. *Network: Computation in Neural Systems* 12: 199–213.
- [15] Fiorani M, Azzi JC, Soares JG, Gattass R (2014) Automatic mapping of visual cortex receptive fields: A fast and precise algorithm. *Journal of Neuroscience Methods* 221: 112–126.
- [16] Pitkow X, Meister M (2012) Decorrelation and efficient coding by retinal ganglion cells. *Nature Neuroscience* 15: 628–635.
- [17] Kolb H (1995) *Simple Anatomy of the Retina*.
- [18] Provis JM, Diaz CM, Dreher B (1998). Ontogeny of the primate fovea: A central issue in retinal development.
- [19] Wagner HJ, Fröhlich E, Negishi K, Collin SP (1998) The eyes of deep-sea fish II. Functional morphology of the retina. *Progress in Retinal and Eye Research* 17: 637–685.
- [20] Straznicky C, Chehade M (1987) The formation of the area centralis of the retinal ganglion cell layer in the chick. *Development (Cambridge, England)* 100: 411–420.
- [21] Yu J, Wang L, Weng SJ, Yang XL, Zhang DQ, et al. (2013) Hyperactivity of ON-Type Retinal Ganglion Cells in Streptozotocin-Induced Diabetic Mice. *PLoS ONE* 8: 1–9.
- [22] O’Regan J (1990) Eye movements and their role in visual and cognitive processes. In: *Eye movements and Reading*, volume 4. pp. 395–453.

- [23] Human brain anatomy and physiology wikipedia Archives - Human Anatomy Charts. URL <https://anatomybody101.com/tag/human-brain-anatomy-and-physiology-wikipedia/>.
- [24] Sanes JR, Masland RH (2015) The types of retinal ganglion cells: Current status and implications for neuronal classification. *Annual Review of Neuroscience* 38: 221-246.
- [25] Nelson R (2007) Visual Responses of Ganglion Cells. *Webvision The Organization of the Retina and Visual System* : 1–61.
- [26] Hartline HK (1938) The response of single optic nerve fibers of the vertebrate eye to illumination of the retina. *American Journal of Physiology* 121: 400–415.
- [27] Barlow HB, Levick WR (1965) The mechanism of directionally selective units in rabbit's retina. *The Journal of Physiology* 178: 477–504.
- [28] Wang GY, Liets LC, Chalupa LM (2001) Unique functional properties of on and off pathways in the developing mammalian retina. *J Neurosci* 21: 4310–4317.
- [29] Purves D, Williams SMSM (2001) *Neuroscience*. Sinauer Associates.
- [30] Michiel Van Wyk, Heinz Wässle WRT (2009) Receptive field properties of ON- and OFF-ganglion cells in the mouse retina. *Visual Neuroscience* 26: 297–308.
- [31] Rodieck RW, Stone J (1965) Analysis of receptive fields of cat retinal ganglion cells. *Journal of Neurophysiology* 28: 833-849.
- [32] Baccus SA, Meister M (2002) Fast and slow contrast adaptation in retinal circuitry. *Neuron* 36: 909–919.
- [33] Kuffler SW (1951) Discharge Patterns and Functional of Mammalian Retina *. *Journal of neurophysiology* .
- [34] Wiesel TN (1960) Receptive fields of ganglion cells in the cat's retina. *The Journal of Physiology* 153: 583–594.
- [35] Enroth-cugell C, Robson JG (1966) The contrast sensitivity of retinal ganglion cells of the cat. *Journal of Physiology* 187: 517–552.
- [36] Wienbar S, Schwartz G (2018) The dynamic receptive fields of retinal ganglion cells. *Progress in Retinal and Eye Research* : 0–1.

- [37] (2012) Overview of fMRI analysis. *Functional Magnetic Resonance Imaging: An Introduction to Methods* 77.
- [38] Neher E, Sakmann B (1992) The patch clamp technique. *Scientific American* 266: 44–51.
- [39] Veitinger S (2011). The Patch-Clamp Technique. URL <https://www.leica-microsystems.com/science-lab/the-patch-clamp-technique/>.
- [40] Henze DA, Borhegyi Z, Csicsvari J, Mamiya A, Harris KD, et al. (2000) Intracellular Features Predicted by Extracellular Recordings in the Hippocampus In Vivo. *Journal of Neurophysiology* 84: 390–400.
- [41] Gross GW, Rieske E, Kreutzberg GW, Meyer A (1977) A new fixed-array multi-microelectrode system designed for long-term monitoring of extracellular single unit neuronal activity in vitro. *Neuroscience letters* 6: 101–5.
- [42] Pine J (1980) Recording action potentials from cultured neurons with extracellular microcircuit electrodes. *Journal of Neuroscience Methods* 2: 19–31.
- [43] Obien MEJ, Deligkaris K, Bullmann T, Bakkum DJ, Frey U (2015) Revealing neuronal function through microelectrode array recordings. *Frontiers in Neuroscience* 9: 423.
- [44] Morin FO, Takamura Y, Tamiya E (2005) Investigating neuronal activity with planar microelectrode arrays: achievements and new perspectives. *Journal of Bioscience and Bioengineering* 100: 131–143.
- [45] Meister M, Wong RO, Baylor DA, Shatz CJ (1991) Synchronous bursts of action potentials in ganglion cells of the developing mammalian retina. *Science (New York, NY)* 252: 939–43.
- [46] Du J, Blanche TJ, Harrison RR, Lester HA, Masmanidis SC (2011) Multiplexed, high density electrophysiology with nanofabricated neural probes. *PLoS ONE* 6: e26204.
- [47] Berdondini L, Bosca A, Nieuws T, Maccione A (2014) Active pixel sensor multi-electrode array for high spatiotemporal resolution. *Nanotechnology and Neuroscience: Nano-Electronic, Photonic and Mechanical Neuronal Interfacing* : 207–238.
- [48] Franks W, Heer F, McKay I, Taschini S, Sunier R, et al. (2003) Cmos monolithic microelectrode array for stimulation and recording of natural neural

- networks. In: TRANSDUCERS '03. 12th International Conference on Solid-State Sensors, Actuators and Microsystems. Digest of Technical Papers (Cat. No.03TH8664). volume 2, pp. 963-966 vol.2.
- [49] Stosiek C, Garaschuk O, Holthoff K, Konnerth A (2003) In vivo two-photon calcium imaging of neuronal networks. *Proceedings of the National Academy of Sciences* 100: 7319–7324.
- [50] Gonzalo H, Pedreira C, Quiari R (2015) Past, present and future of spike sorting techniques. *Brain Research Bulletin* 119: 106–117.
- [51] Hurwitz C, Sorbaro M (2018) Scaling Spike Detection and Sorting for Next Generation : 1–14.
- [52] Hermle T, Schwarz C, Bogdan M (2004) Employing ica and som for spike sorting of multielectrode recordings from cns. *Journal of Physiology-Paris* 98: 349 - 356.
- [53] Quiroga RQ, Nadasdy Z, Ben-Shaul Y (2004) Unsupervised spike detection and sorting with wavelets and superparamagnetic clustering. *Neural Computation* 16: 1661-1687.
- [54] Harris K, Henze D, Csicsvari J, Hirase H, Buzsáki G (2000) Accuracy of Tetrode Spike Separation as Determined by Simultaneous Intracellular and Extracellular Measurements, volume 84. 401–414 pp.
- [55] Wood F, Goldwater S, Black MJ (2006) A non-parametric Bayesian approach to spike sorting. *Conference proceedings : Annual International Conference of the IEEE Engineering in Medicine and Biology Society IEEE Engineering in Medicine and Biology Society Conference* 1: 1165–8.
- [56] Hilgen G, Sorbaro M, Pirmoradian S, Muthmann JO, Kepiro IE, et al. (2017) Unsupervised Spike Sorting for Large-Scale, High-Density Multielectrode Arrays. *Cell Reports* 18: 2521–2532.
- [57] Lebedev MA, Nicolelis MA (2006) Brain–machine interfaces: past, present and future. *Trends in Neurosciences* 29: 536 - 546.
- [58] Mulas M, Massobrio P, Martinoia S, Chiappalone M (2010) A simulated neuro-robotic environment for bi-directional closed-loop experiments. *Paladyn, Journal of Behavioral Robotics* 1.
- [59] Park I, Paiva ARC, DeMarse TB, Príncipe JC (2008) An efficient algorithm for continuous time cross correlogram of spike trains. *Journal of Neuroscience Methods* 168: 514–523.

- [60] Baden T, Berens P, Franke K, Román Rosón M, Bethge M, et al. (2016) The functional diversity of retinal ganglion cells in the mouse. *Nature* 529: 345–350.
- [61] Angotzi GN, Boi F, Lecomte A, Miele E, Malerba M, et al. (2018) Sinaps: an implantable active pixel sensor cmos-probe for simultaneous large-scale neural recordings. *Biosensors and Bioelectronics* .

